International Journal of Heat and Fluid Flow 104 (2023) 109236

Contents lists available at ScienceDirect

International Journal of Heat and Fluid Flow

journal homepage: www.elsevier.com/locate/ijhff

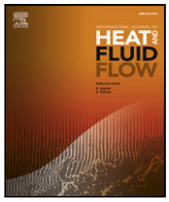

# The acoustic signature of a rudder in the wake of a propeller: Comparison between infinite and semi-infinite approximations

Antonio Posa [a,*], Riccardo Broglia [a], Elias Balaras [b], Mario Felli [a]

[a] CNR-INM, Institute of Marine Engineering, National Research Council of Italy, Via di Vallerano 139, 00128 Roma, Italy
[b] The George Washington University, Department of Mechanical and Aerospace Engineering, 800 22nd Street NW, Washington, DC 20052, USA

ARTICLE INFO

*Keywords:*
Large-Eddy simulation
Acoustic analogy
Ffowcs–Williams and Hawkings equation
Propeller–rudder interaction
Immersed boundary method

ABSTRACT

The acoustic analogy is adopted to reconstruct the sound pressure levels from a propeller–rudder system, using the database of instantaneous realizations of the solution from Large-Eddy Simulations, conducted on a cylindrical grid of 3.8 billion points. Results are compared across incidence angles and rudder geometries, approximated by hydrofoils of infinite and semi-infinite spanwise extents. The latter parameter does not affect significantly the acoustic pressure at no incidence, but its influence grows for increasing angles. Actually, trends are different at inner and outer radii. In the vicinity of the propeller wake, the acoustic signature is dominated by the non-linear sources of sound and is higher when the infinite approximation of the rudder geometry is considered, due to the massive separation affecting the suction side of the hydrofoil. In contrast, moving away along the radial direction the lead goes to the linear sources of sound on the surface of the hydrofoil, which are higher in the case of the semi-infinite approximation of the rudder. Surprisingly, separation phenomena, more significant on the suction side of the infinite hydrofoil, result in a lower loading component of the sound, at least in the range of low frequencies considered in the present study, maybe due to a shift of the acoustic signature of the system towards higher frequencies.

## 1. Introduction

Naval propulsion is a growing source of underwater noise (Merchant 2019, Chou et al. 2021, Vakili et al. 2021, Smith and Rigby 2022). This is an important issue, especially due to its detrimental impact on the environment, negatively affecting the life of marine species (Di Franco et al. 2020, Masud et al. 2020, Wang et al. 2021). Unfortunately, the analysis of noise from marine propulsion poses several challenges to both experiments and computations. Experiments are definitely important, but they face a number of problems, especially in terms of noise measurement. As demonstrated in the recent study carried out by Tani et al. (2020), dealing with a marine propeller in open-water conditions, acoustic measurements conducted in different facilities usually result in a significant scatter of the results, due especially to background noise, reverberations from walls and self-induced noise from hydrophones. Also the acoustic analysis based on numerical approaches is challenging, because of its substantial computational cost, tied to the need of resolving a wide range of scales, not only in the vicinity of propellers, but also in their wake. The theoretical study by Ianniello (2016) pointed out that only eddy-resolving methodologies, able to keep very fine levels of resolution across the downstream development of the wake flow, are suitable to provide data useful for an accurate investigation of the hydro-acoustics of marine propellers.

To date, most computational studies focusing on underwater radiated noise (URN) from marine propellers rely on Reynolds-averaged Navier–Stokes (RANS) approaches (Lidtke et al., 2015, 2016, 2019; Sakamoto and Kamiirisa, 2018; Sezen and Kinaci, 2019; Sezen et al., 2021b,c,d; Chen et al., 2022; McIntyre et al., 2022). Unfortunately, as claimed by Ianniello et al. (2013, 2014), RANS is overly dissipative to properly account for all components of the acoustic signature. In particular, RANS does not explicitly resolve turbulence, affecting both the linear component of the sound coming from the surface of bodies as well as the non-linear one coming from their wake. In addition, RANS is not designed to properly reproduce the instability phenomena affecting the large wake structures shed by marine propellers, which are important non-linear sources of sound. A number of works using more accurate, eddy-resolving approaches, such as Detached-Eddy Simulation (DES) or wall-modeled Large-Eddy Simulation (LES), are available in the literature (Cianferra et al. 2018, 2019a,b, Viitanen et al. 2018, Ianniello and Testa 2019, Qin et al. 2019, Cianferra and Armenio 2021, Hu et al. 2021a, Sezen et al. 2021a, Testa et al. 2021, Petris et al. 2022, Sezen and Atlar 2022b, Lidtke et al. 2022). However,

* Corresponding author.
*E-mail addresses:* antonio.posa@cnr.it (A. Posa), riccardo.broglia@cnr.it (R. Broglia), balaras@gwu.edu (E. Balaras), mario.felli@cnr.it (M. Felli).

https://doi.org/10.1016/j.ijheatfluidflow.2023.109236
Received 8 May 2023; Received in revised form 15 September 2023; Accepted 18 October 2023
Available online 24 October 2023

they share the same limitations with RANS in terms of grid resolution, especially downstream of propellers in their wake flow. Furthermore, the near wall flow is modeled or resolved by a RANS approach. This is a problem, since the ability of resolving accurately the near wall flow and in particular the pressure fluctuations on the surface of immersed bodies is important for reproducing correctly the acoustic signature associated with the loading component of sound. This issue was recently addressed in the work by Liefvendahl et al. (2022), where a technique for reconstructing the near-wall pressure fluctuations from wall-modeled LES computations is proposed. Today, only a handful number of studies on the sound from marine propellers, relying on wall-resolved LES (see Keller et al. 2018, Kimmerl et al. 2021, Posa et al. 2022c), have been reported.

Most of the above studies have been conducted with marine propellers operating in open-water conditions, neglecting the interaction with neighboring bodies, which has an important impact on URN. Only a few exceptions can be found to date. For instance, Felli et al. (2014a,b, 2015) analyzed experimentally the sound coming from a NACA0020 hydrofoil, mimicking a rudder working in the wake of the four-bladed INSEAN E779A propeller. Kimmerl et al. (2021) reported LES computations in open-water configurations as well as three behind-ship conditions of realistic test-cases (the ProNoVi Target Case, the SCHOTTEL Reference Case 1 and the SCHOTTEL Reference Case 2). This is one of the most detailed studies on the acoustics of propeller–rudder systems in realistic configurations. A limitation, however, is the use of the porous formulation of the acoustic analogy (Di Francescantonio, 1997). This approach carries some issues, as the impossibility to separate the linear and non-linear components of sound as well as the generation of spurious noise, associated with the end cap problem. In more recent studies, Zhou et al. (2021a,b, 2022, 2023) suggested strategies to mitigate this issue. A number of computational studies considered the full ship system, with the advantage of reproducing more realistically the actual working conditions of propellers (Bensow and Liefvendahl 2016, Guo et al. 2021, Ku et al. 2021, Ge et al. 2022, Kim and Kinnas 2022, Sezen and Atlar 2022a, Kimmerl and Abdel-Maksoud 2023, Yu et al. 2023). This strategy spreads the available resources across a much wider computational domain, with detrimental effects on resolution. However, the recent study by Kim et al. (2023) addresses this issue by resolving the LES equations only in a reduced region, dominated by the propeller, while adopting RANS in the rest of the computational domain.

In our recent studies (Posa et al., 2022b,d, 2023), we reported wall-resolved LES computations of a propeller working upstream of a hydrofoil of infinite spanwise extent, mimicking a rudder across a range of incidence angles. The level of resolution goes beyond what is available in the literature, thanks to a cylindrical grid consisting of about 3.8 billion points, where all computational resources are focused on reproducing the dynamics of the flow across the propeller–rudder system. We found that the interaction between the propeller and the downstream rudder has important effects on the acoustic signature, dominating the sound pressure levels ($SPLs$) and producing higher values than in open-water conditions, especially in the direction normal to the surface of the hydrofoil, as a result of the impingement of the hub and tip vortices shed by the propeller on the surface of the hydrofoil. However, a limitation of those works is the infinite extent of the hydrofoil, which did not allow us to take into account the end effects arising during the operation of actual rudders. In the present study, we address this limitation, by mimicking more realistically the geometry of the downstream rudder by means of a semi-infinite hydrofoil (Posa, 2022, 2023). Direct comparisons with our earlier works considering an infinite hydrofoil (Posa et al., 2022b,d) will allow isolating the impact of the end effects on the acoustic signature.

The present analysis, as in our earlier works, is based on the acoustic analogy (Lighthill, 1952). The acoustic signature is studied here as a function of both the incidence angle of the hydrofoil and its spanwise extent, through a comparison of the two simulated approximations of the rudder geometry, which is the novelty of this study from the earlier ones. The infinite approximation of rudders was adopted in several works dealing with propeller–rudder interaction (Li 1996, Felli et al. 2009, 2011, 2013, 2014a,b, Felli and Falchi 2011, Felli 2020, Hu et al. 2019, 2021b, Wang et al. 2019). The aim of the present study is to assess its limitations in terms of prediction of the acoustic signature of the overall system.

This manuscript is organized in a discussion of the methodology (Section 2), setup (Section 3), results of the acoustic analysis (Section 4) and conclusions (Section 5).

## 2. Methodology

### 2.1. Governing equations of the fluid dynamics

The flow was reproduced by the solution of the filtered Navier–Stokes equations for incompressible flows in non-dimensional form:

$$\frac{\partial \tilde{u}_i}{\partial x_i} = 0, \quad i = 1,2,3, \tag{1}$$

$$\frac{\partial \tilde{u}_i}{\partial t} + \frac{\partial \tilde{u}_i \tilde{u}_j}{\partial x_j} = -\frac{\partial \tilde{p}}{\partial x_i} - \frac{\partial \tau_{ij}}{\partial x_j} + \frac{1}{Re}\frac{\partial^2 \tilde{u}_i}{\partial x_j^2} + f_i, \quad i,j = 1,2,3, \tag{2}$$

where $\tilde{u}_i$ and $\tilde{p}$ are the filtered velocity and pressure, respectively, $x_i$ the coordinate in space, $t$ time, $\tau_{ij}$ the subgrid scale (SGS) stress tensor, $Re$ the Reynolds number and $f_i$ a forcing term, utilized to represent the action of the bodies on the flow in the framework of an Immersed-Boundary (IB) methodology. The Reynolds number, $Re = UL/\nu$, comes from scaling the dimensional Navier–Stokes equations using the reference velocity, $U$, the reference length, $L$, and the density of the fluid, $\rho$, while $\nu$ is the kinematic viscosity of the fluid.

In this study, as typical in LES, the deviatoric part of the SGS stress tensor is assumed proportional to the deformation tensor of the resolved velocity field, $\widetilde{S}_{ij}$, through the eddy-viscosity, $\nu_t$:

$$\tau_{ij}^d = \tau_{ij} - \frac{1}{3}\tau_{kk}\delta_{ij} = -2\nu_t \widetilde{S}_{ij}, \quad \widetilde{S}_{ij} = \frac{1}{2}\left(\frac{\partial \tilde{u}_i}{\partial x_j} + \frac{\partial \tilde{u}_j}{\partial x_i}\right), \quad i,j = 1,2,3, \tag{3}$$

where $\tau_{kk}$ is the trace of the SGS tensor and $\delta_{ij}$ is the Kronecker delta. This assumption reduces the problem of turbulence closure to modeling of a single variable, the eddy viscosity. In the present study, $\nu_t$ was computed using the wall-adaptive local eddy-viscosity (WALE) model by Nicoud and Ducros (1999), which was found suitable to this class of flows, as demonstrated in our earlier works, including also validations against experiments (Posa et al., 2019a,b, 2022a).

The enforcement of the no-slip boundary condition on the surface of the bodies immersed within the flow was achieved using an IB technique. In IB methods the Navier–Stokes equations are resolved on an Eulerian grid, which discretizes the computational domain and is not required to fit the geometry of the bodies. Meanwhile, the discretization of the surface of the immersed boundaries is based on Lagrangian grids, which are immersed within the Eulerian grid and are free to move across the computational domain during the advancement in time of the solution. The points of the Eulerian grid are tagged as *fluid*, *solid* and *interface*, depending on their position relative to the Lagrangian grids. The boundary conditions on the surface of the bodies are enforced through the term $f_i$ within the momentum equation. It is computed as:

$$f_i = \frac{U_i - \tilde{u}_i}{\Delta t} - RHS_i, \quad i = 1,2,3, \tag{4}$$

where $U_i$ is the boundary condition to be enforced, $\tilde{u}_i$ the filtered velocity along the direction $i$ from the numerical solution of the flow at the last time level, $\Delta t$ the step of advancement in time of the numerical solution and $RHS_i$ the sum of the convective, viscous and SGS terms of the momentum equation, resolved explicitly. At the fluid points of the Eulerian grid no condition is enforced, so $f_i = 0$. At the solid points $U_i$ is equal to the velocity of the body immersed within the

flow. At the interface points, between the solid and fluid regions of the computational domain, $U_i$ comes from a linear reconstruction of the solution in the direction normal to the surface of the bodies, using as boundary conditions the no-slip requirement on them and the solution at the fluid points in the vicinity of the particular interface point. More details dealing with the present IB technique can be found in the work by Yang and Balaras (2006).

The Navier–Stokes equations were resolved on a staggered grid in cylindrical coordinates. Second-order, central finite-differences were utilized to discretize all derivatives in space. The advancement in time was based on a fractional-step method (Van Kan, 1986). For the discretization in time of all convective, viscous and SGS terms of derivatives in the radial and axial directions the explicit, three-step Runge–Kutta (RK3) scheme was utilized. To relax the stability restrictions, arising at the axis of the cylindrical grid, all terms of azimuthal derivatives were discretized using the implicit Crank–Nicolson scheme. At each time-substep, the momentum equation was provisionally advanced in time without enforcement of the continuity requirement, giving the provisional velocity, $\tilde{u}_i^*$. Then, this non divergence-free velocity field was projected onto a solenoidal field by means of the gradient of the scalar pseudo-pressure, $\varphi$:

$$\tilde{u}_i^l = \tilde{u}_i^* - \alpha_l \Delta t \frac{\partial \varphi^l}{\partial x_i}, \tag{5}$$

where $l$ is the substep index, in this case ranging from 1 to 3, while $\alpha_l$ is the coefficient of the particular scheme of discretization in time (in this case RK3) at the substep $l$. The enforcement of the continuity condition for $\tilde{u}_i^l$ resulted in a hepta-diagonal Poisson problem for $\varphi$:

$$\frac{\partial^2 \varphi^l}{\partial x_i^2} = \frac{1}{\alpha_l \Delta t} \frac{\partial \tilde{u}_i^*}{\partial x_i}. \tag{6}$$

This was reduced to a penta-diagonal system of equations in the radial and axial directions for each azimuthal slice of the cylindrical grid by using trigonometric transformations along the azimuthal direction. Then, each penta-diagonal Poisson problem was inverted by means of the direct solver developed by Rossi and Toivanen (1999). The computation of the pseudo-pressure allowed correcting the velocity field through Eq. (5), to meet continuity. To satisfy the momentum equation at the time-substep $l$, the pressure field was then updated as follows:

$$\tilde{p}^l = \tilde{p}^{l-1} + \varphi^l - \frac{\alpha_l \Delta t}{2Re} \frac{\partial^2 \varphi^l}{\partial x_i^2}. \tag{7}$$

As demonstrated by Yang and Balaras (2006), the overall Navier–Stokes solver is second-order accurate in both space and time and was utilized in a variety of practical flow problems, including also naval hydrodynamics (Posa and Balaras, 2016, 2018, 2020).

Note that in the following discussion, unless otherwise stated, only resolved quantities will be provided. Therefore, the notation $\tilde{\cdot}$ will be omitted.

### 2.2. Computation of the acoustic pressure

The computation of the acoustic pressure was based on the acoustic analogy, which assumes that the acoustic phenomena have a negligible influence on the fluid dynamics (Lighthill, 1952). This means that the influence of the acoustic phenomena on the flow physics is neglected. Also the effects of sound convection and refraction within the turbulent flow are not accounted for. Within this assumption the flow is treated as a collection of acoustic sources and the acoustic pressure is reconstructed through the wave theory. As a result, the acoustic analysis is performed by post-processing the database generated through the solution of the Navier–Stokes equations. Although the acoustic analogy, exploited in the present work, is strictly correct in the acoustic far field, it was utilized successfully in naval hydrodynamics to conduct a number of studies on the acoustic near field (Ianniello et al. 2014, Kimmerl et al. 2021, Ge et al. 2022, Lidtke et al. 2022, Sezen and Atlar 2023), where the results were in good agreement with physical experiments.

We computed in post-processing all terms of the integral formulation of the Ffowcs-Williams & Hawkings equation (Ffowcs-Williams and Hawkings, 1969):

$$\begin{aligned} 4\pi \hat{p}(\boldsymbol{x},t) = {} & \frac{\partial}{\partial t}\int_S \left[\frac{\rho_0 v_n}{r|1-\mathcal{M}_r|}\right]_{\mathcal{T}} dS + \frac{1}{C}\frac{\partial}{\partial t}\int_S \left[\frac{p'\hat{n}_i\hat{r}_i}{r|1-\mathcal{M}_r|}\right]_{\mathcal{T}} dS + \\ & \int_S \left[\frac{p'\hat{n}_i\hat{r}_i}{r^2|1-\mathcal{M}_r|}\right]_{\mathcal{T}} dS + \frac{1}{C^2}\frac{\partial^2}{\partial t^2}\int_{\mathcal{V}} \left[\frac{\mathcal{L}_{rr}}{r|1-\mathcal{M}_r|}\right]_{\mathcal{T}} dV + \\ & \frac{1}{C}\frac{\partial}{\partial t}\int_{\mathcal{V}} \left[\frac{3\mathcal{L}_{rr}-\mathcal{L}_{kk}}{r^2|1-\mathcal{M}_r|}\right]_{\mathcal{T}} dV + \int_{\mathcal{V}} \left[\frac{3\mathcal{L}_{rr}-\mathcal{L}_{kk}}{r^3|1-\mathcal{M}_r|}\right]_{\mathcal{T}} dV, \quad i=1,2,3, \end{aligned} \tag{8}$$

where $\hat{p}$ is the acoustic pressure, $\rho_0$ the reference density, $v_n$ the velocity component of the elemental surface $dS$ in the outward normal direction, defined by the normal unit vector of components $\hat{n}_i$, $p'$ is the fluctuation in time of the hydrodynamic pressure, $r$ the magnitude of the vector of components $r_i = x_i - y_i$, where $x_i$ and $y_i$ are the coordinates in the direction $i$ of the positions of the receiver and the source, respectively, while $\hat{r}_i$ is the $i$-component of the corresponding unit vector. $\mathcal{M}_r$ is the Mach number of the flow in the direction of the vector $\boldsymbol{r}$, $C$ the speed of sound in the fluid and $\mathcal{L}_{ij}$ the Lighthill tensor, defined as:

$$\mathcal{L}_{ij} = \rho u_i u_j + \left[(p-p_0) - C^2(\rho-\rho_0)\right]\delta_{ij} - \sigma_{ij}, \quad i,j=1,2,3, \tag{9}$$

where $p_0$ is the reference pressure and $\sigma_{ij}$ the viscous stress tensor. In Eq. (8), $\mathcal{L}_{rr} = \mathcal{L}_{ij}\hat{r}_i\hat{r}_j$, while $\mathcal{L}_{kk}$ is the trace of the Lighthill tensor.

The terms in the right hand side of Eq. (8) are integrated over a surface, $\mathcal{S}$, and a volume, $\mathcal{V}$. In the present study the direct approach to the Ffowcs-Williams & Hawkings acoustic analogy was adopted, which means that the surface of the bodies immersed within the flow was selected as $\mathcal{S}$, while the volume of integration was chosen to encompass all important sources of sound, having as inner boundary the surface of the bodies and as a outer boundary a cylinder centered at the axis of the propeller. More details will be provided in Section 3.

The surface and volume integrals in Eq. (8) should be computed at the emission time $\mathcal{T}$, differing from the time $t$, due to the time delay associated with the propagation of sound from the source to the receiver, of positions $\boldsymbol{y}$ and $\boldsymbol{x}$, respectively:

$$\mathcal{T} = t - \frac{r}{C} = t - \frac{|\boldsymbol{x}(t) - \boldsymbol{y}(\mathcal{T})|}{C}. \tag{10}$$

The time delay causes a practical complication in the post-processing of the data. However, in the class of flows considered in the present study, it is negligible, due to the large value of $C$, in comparison with the typical velocities of propellers, as also verified in earlier studies dealing with the same subject (Ianniello et al. 2013, Cianferra et al. 2019a).

In the following discussion of the results, the components of the acoustic pressure will be distinguished between linear and non-linear terms, corresponding to the surface and volume integrals of Eq. (8), respectively. In particular, the first surface integral at the right hand side is the *monopole* or *thickness* term, arising from the displacement of fluid by the bodies immersed within the flow, the second and the third surface integrals are the *dipole* or *loading* terms, originating from pressure fluctuations on the surface of the bodies, while the three volume integrals are the *quadrupole* terms and originate from vorticity and turbulence within the flow field. Below we will show that, while the thickness terms are never important in the present flow problem, the loading or the quadrupole terms have the lead on the acoustic signature of the system, depending on the radial position of the receiver.

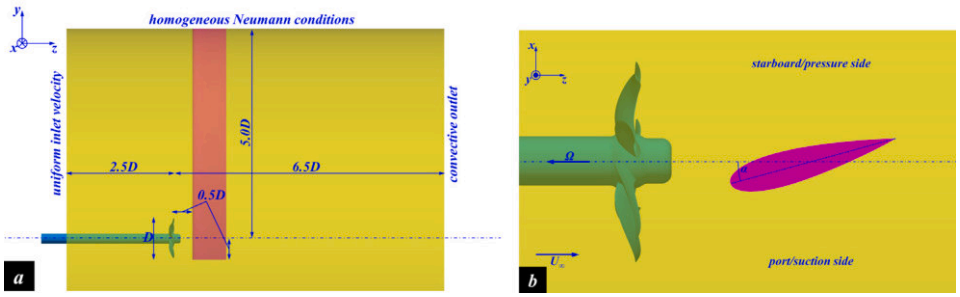


**Fig. 1.** Visualization of the geometry of the problem, within the computational domain, represented in yellow color: global lateral view in the left panel (*a*) and detailed top view in the right panel (*b*). Case of the hydrofoil at an incidence angle $\alpha = 15°$. For interpretation of the references to color in this figure legend, the reader is referred to the webversion of this article.

## 3. Computational setup

### 3.1. Definition of the flow problem

LES computations were conducted on a system consisting of the seven-bladed INSEAN E1658 propeller and a downstream NACA0020 hydrofoil, mimicking a rudder of semi-infinite spanwise extent (Fig. 1). On the side of positive $y$ coordinates the latter extends up to the boundary of the computational domain, while on the opposite side its tip is placed at $y/D = -0.5$, where $D$ is the diameter of the propeller. The chord length of the hydrofoil was selected equal to $c = 0.833D$. These computations were conducted for comparison with those in our earlier studies (Posa and Broglia, 2021, 2022a,b,c), dealing with a similar system, but characterized by a hydrofoil of infinite spanwise extent, spanning the whole computational domain, with the purpose of removing the influence of its end effects and isolating the phenomena associated with the interaction between the propeller wake and the port/starboard sides of the hydrofoil. The geometries of the infinite and semi-infinite hydrofoils will be indicated below as *A* and *B*, respectively.

Both hydrofoils were simulated at four incidence angles. In the baseline configuration at no incidence the hydrofoil was aligned with the free-stream and the axis of the upstream propeller. Its leading edge was placed at $0.5D$ downstream of the propeller plane. Incidence conditions were produced by rotating the hydrofoil around its mid chord, at angles of 5°, 10° and 15°. In particular, the case at an incidence of 15° is shown in Fig. 1. Hereafter, these four configurations of incidence angle will be indicated as ***I*00**, ***I*05**, ***I*10** and ***I*15**, respectively.

The propeller was simulated at an advance coefficient equal to:

$$J = V/nD = 0.65, \tag{11}$$

where $V$ is the advance velocity, equivalent in this case to the free-stream velocity, $U_\infty$, while $n$ is its frequency of rotation. The model-scale Reynolds number considered in all simulations was equal to:

$$Re_p = \frac{b_{0.7R}\sqrt{(2\pi n\, 0.7R)^2 + V^2}}{\nu} \approx 3.1 \times 10^5, \tag{12}$$

where $b_{0.7R}$ is the chord of the propeller blades at 70% of $R = D/2$, while $\nu$ is the kinematic viscosity of water. We selected these particular values of advance coefficient and model-scale Reynolds number, since in our earlier studies (Posa et al., 2019a, 2022a,c) the same LES-IB approach was validated on the isolated INSEAN E1658 propeller, working in the same conditions, against both fluid dynamic and hydro-acoustic measurements (Felli and Falchi, 2018). Although experiments matching exactly the same working conditions of the propeller–rudder system are not available, the present results are in good qualitative agreement with measurements and computations conducted on similar systems (Felli and Falchi 2011, Hu et al. 2019, Wang et al. 2019, Felli 2020).

### 3.2. Computational domain and grid resolution

All computations were conducted within a cylindrical domain, centered at the axis of the propeller (Fig. 1). The inlet section was placed $2.5D$ upstream of the propeller plane, the outlet section $6.5D$ downstream, while the radial extent of the domain was equivalent to $5.0D$. The origin of the streamwise coordinates was placed on the propeller plane. At the inlet section, Dirichlet conditions were enforced, imposing a uniform axial velocity, equal to $U_\infty$. This should be acknowledged as a limitation of the present study, since turbulence ingested by a propeller, for instance operating in the wake of the hull of a ship, is able to affect the pressure fluctuations on its surface, the instability of its wake and in turn its acoustic signature. At the outlet section, convective conditions were utilized for all three velocity components, adopting as convective velocity $U_\infty$. At the lateral cylindrical boundary free-stream conditions were mimicked by imposing homogeneous Neumann conditions for all velocity components. Neumann conditions were also utilized for both pressure and eddy-viscosity across all boundaries of the cylindrical domain.

The use of an IB methodology allowed us adopting a regular, cylindrical (Eulerian) grid to discretize the computational domain (Fig. 2). It was composed of an overall number of 3.8 billion points: $900 \times 2050 \times 2050$, distributed across the radial, azimuthal and axial directions, respectively. This is the same grid we utilized in our earlier studies (Posa and Broglia, 2021, 2022a,b,c), dealing with an infinite hydrofoil working in the wake of the INSEAN E1658 propeller, as well as with the same propeller in isolated conditions (Posa et al., 2022a). For the latter configuration we reported detailed comparisons with the Particle Imaging Velocimetry (PIV) experiments by Felli and Falchi (2018). In addition, the present grid is even finer than the 840 million points mesh we adopted for the comparisons with acoustic measurements, reported in Posa et al. (2022c).

The radial and axial grids were stretched, as shown in Fig. 2, with the purpose of clustering points in the vicinity of the hydrofoil, the propeller and its wake. In particular, the radial grid was uniform along the span of the propeller blades, up to $r/D = 0.6$ ($\Delta r/D = 8.0 \times 10^{-4}$). It was stretched smoothly between $0.6 < r/D < 0.8$, taking into account that the interaction of the propeller wake with the hydrofoil causes the spanwise expansion of the former. Then, coarsening was accelerated up to the lateral boundary of the domain, to save computational resources. The axial grid was uniform across the propeller blades ($\Delta z/D = 5.3 \times 10^{-4}$), then it was stretched downstream of them, achieving again a uniform resolution across the hydrofoil ($\Delta z/D = 1.5 \times 10^{-3}$). Further downstream, grid stretching was again adopted, but with the purpose of resolving accurately the wake development up to $z/D = 4.5$. Then, coarsening was accelerated up to the outflow boundary of the cylindrical domain. The near wall resolution on both propeller and hydrofoil was equivalent to about 5 viscous lengths.

The use of a cylindrical grid, in comparison with a Cartesian one, is more suitable to the particular flow problem for saving computational

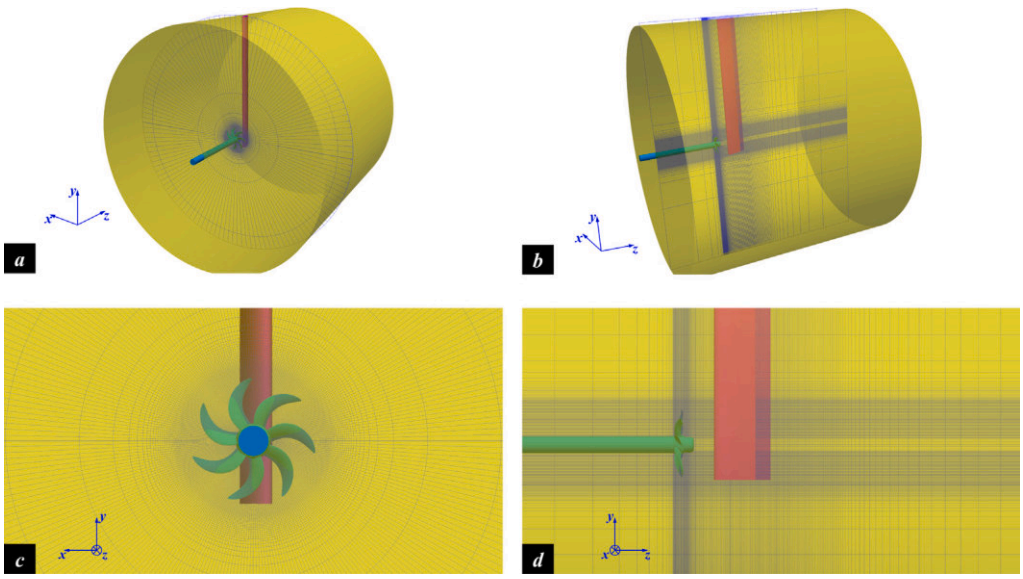


**Fig. 2.** Visualizations of cross-stream (*a* and *c*) and meridian (*b* and *d*) slices of the cylindrical grid. One of every 256 points shown in the global views (*a* and *b*). One of every 64 points shown in the detailed views (*c* and *d*).

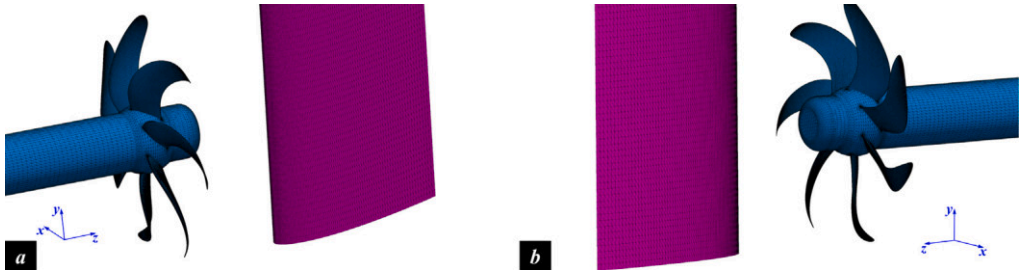


**Fig. 3.** Visualizations of the Lagrangian grids discretizing the surfaces of propeller and hydrofoil: views from the port (*a*) and starboard (*b*) sides.

resources and clustering points in the region of interest. Although the angular spacing of the azimuthal grid was uniform, this choice was indeed equivalent to a finer linear spacing towards inner radii, where the propeller and its wake were placed. In other words, the cylindrical topology of the grid inherently allowed clustering Eulerian points in the region of large gradients of the solution, while stretching was achieved moving towards the lateral boundary of the domain. In particular, at 70% of the radial extent of the propeller, the grid resolution was equivalent to $0.7R\Delta\vartheta/D = 1.1 \times 10^{-3}$, where $\Delta\vartheta$ is the constant angular spacing of the cylindrical grid, so $0.7R\Delta\vartheta$ is its linear azimuthal spacing at the particular radial location.

In IB methods the geometry of the bodies immersed within the flow is represented by using Lagrangian grids, discretizing their surfaces. For the propeller and the hydrofoil, grids consisting of 166,000 and 80,000 triangles were adopted, respectively (Fig. 3). Taking advantage of the features of IB methodologies, the rotation of the propeller during the advancement in time of the numerical solution was accounted for by rotating its Lagrangian grid, based on the angular speed corresponding to the simulated advance coefficient.

The resolution in time of all computations was prescribed by the stability requirements associated with the Runge–Kutta scheme adopted for the explicit discretization of all terms of radial and axial derivatives of the momentum equation. All computations were carried out enforcing a constant value of the Courant–Friedrichs–Lewy number, equal to 1. The resulting, average time step of the simulations was equivalent to a rotation of about 0.05°. So, the resolution in time, tied to that in space for stability reasons, was also very fine.

All present computations, starting from conditions of uniform flow, were initially advanced in time during two flow-through times, with the purpose of removing the memory of initial conditions and achieving a statistically steady wake flow. Then, time-averaged statistics, indicated below as $\bar{\cdot}$, were computed at run time, including within the statistical sample all instantaneous realizations of the solution, during 10 additional rotations of the propeller. All simulations were carried out by splitting the overall flow problem into cylindrical subdomains, spread across 1024 cores of a distributed-memory cluster in a High Performance Computing environment. Calls to MPI libraries were utilized for communications across subdomains. The overall cost of the computations conducted in the framework of this study (dealing with the semi-infinite hydrofoil) was equivalent to about 10 million core-hours.

### 3.3. Analysis of the acoustic signature

The analysis of the acoustic signature utilized hydrophones placed at the streamwise locations $z/D = 1.0$ and $z/D = 4.0$ and the radial locations $r/D = 1.5$ and $r/D = 12$. They were distributed across the azimuthal direction, with a uniform spacing of 5°, with the aim of increasing the size of the statistical sample and analyzing the influence of the hydrofoil and its orientation on the directivity of the acoustic signature of the overall system. Eventually, 216 hydrophones were considered in this study: 72 hydrophones at the coordinates ($r/D = 1.5$, $z/D = 1.0$), ($r/D = 1.5$, $z/D = 4.0$) and ($r/D = 12$, $z/D = 1.0$), respectively. For clarity of the following discussion, it should be noted that the hydrophones aligned with the axis of positive (negative) $x$ coordinates, placed on the starboard (port) side of the hydrofoil, are characterized by an azimuthal coordinate $\vartheta = 0°$ ($\vartheta = 180°$), while those aligned with the axis of positive (negative) $y$ coordinates, placed

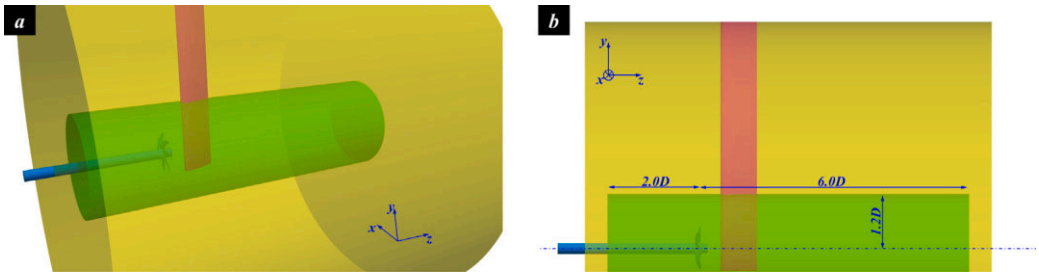


**Fig. 4.** Visualizations of the cylindrical control volume utilized for the acoustic analysis (in green) within the computational domain (in yellow): isometric view (*a*) and lateral view (*b*). For interpretation of the references to color in this figure legend, the reader is referred to the webversion of this article.

on the top (bottom) side are characterized by an azimuthal coordinate $\vartheta = 90°$ ($\vartheta = 270°$).

Results will be reported in decibel (dB) as sound pressure levels:

$$SPL = 20log_{10}\left[A_{FFT}(\hat{p})/\hat{p}_0\right], \tag{13}$$

where $A_{FFT}(\hat{p})$ is the amplitude at a particular frequency of the Fast Fourier Transform (FFT) of the local acoustic pressure, while $\hat{p}_0$ is the reference acoustic pressure, assumed equal to $1\mu Pa$, as typical for URN. Below, the results for $SPLs$ will be provided in third-octave bands, centered at the frequencies $0.5f_s$, $1.0f_s$, $2.0f_s$, $0.5f_b$, $1.0f_b$, $2.0f_b$, $4.0f_b$ and $8.0f_b$, where $f_s$ and $f_b$ are the shaft and blade frequencies, respectively.

As discussed above in Section 2, for the acoustic analysis the integral formulation of the Ffowcs-Williams & Hawkings acoustic analogy was exploited. The volume, quadrupole terms were computed within a cylindrical domain (indicated in green in Fig. 4), centered at the axis of the propeller and having a radial extent equivalent to $1.2D$, in order to include all important sources of sound within the wake of the system. The upstream boundary of the control volume was placed at $2.0D$ from the propeller plane, while the downstream boundary at $6.0D$. The surface, linear terms were computed over the surface of the Lagrangian grids representing the propeller and the hydrofoil, by extrapolation on them of the numerical solution on the Eulerian grid. For coherence with the choice of the control volume, only the elements of the Lagrangian grids of both infinite and semi-infinite hydrofoils with centroids of spanwise coordinate $|y| < 1.2D$ were considered for the computation of the surface integrals of Eq. (8), excluding those placed outside the volume of integration.

## 4. Results

### 4.1. Comparisons across grid resolutions

To provide information about grid dependence of the results, some comparisons are reported between resolutions corresponding to the current grid and the one adopted by Posa et al. (2020). It should be noted that these comparisons deal with the case of the infinite hydrofoil at 0° incidence, for which computations were performed on cylindrical grids consisting of both 1026 and 2050 points in the azimuthal direction, which is practically the one orthogonal to the surface of the hydrofoil. The two grids share the radial and streamwise resolutions. Data are not available for additional configurations, due to computational cost limitations.

The top panels of Fig. 5 deal with the distribution of the time-averaged pressure coefficient on the surface of the hydrofoil at (*a*) $y/D = 0.0$ and (*b*) $y/D = 0.5$. The pressure coefficient was defined as $c_p = (p - p_\infty)/(0.5\rho U_\infty^2)$, where $p_\infty$ and $U_\infty$ are the free-stream pressure and velocity, respectively. On the horizontal axis, $z_c/c$ represents the streamwise coordinate across the hydrofoil as a fraction of its chord length. Note that in Fig. 5*a* the distributions on the port and starboard sides of the hydrofoil overlap, while this is not the case in Fig. 5*b*, due to the asymmetry generated by the wake of the propeller. The agreement between resolutions is very close, pointing also to the significant spanwise gradients experienced by the hydrofoil under the action of the flow coming from the propeller.

Comparisons dealing with the root-mean-squares in time of the pressure coefficient are provided in the bottom panels of Fig. 5, referring to the same locations over the surface of the hydrofoil. As expected, the deviations between resolutions are more evident than on the first-order statistics, but they keep quite small. Although it should be acknowledged that an additional increase of the resolution would be helpful to verify the achievement of grid independence on the present (fine) grid, this was not possible, due to the limitation of available computational resources.

Additional comparisons dealing with the streamwise skin-friction coefficient are reported in the top panels of Fig. 6. This was defined as $c_{fz} = \tau_{wz}/(0.5\rho U_\infty^2)$, where $\tau_{wz}$ is the wall shear stress, computed in the streamwise direction, that is the $z$ direction in the adopted frame of reference. Also in this case the agreement between resolutions is quite satisfactory, albeit showing the potential benefit of an additional increase of the number of points within the boundary layer. A similar comparison is reported in the bottom panels of Fig. 6, where the spanwise skin-friction coefficient is considered. It is defined as $c_{fy} = \tau_{wy}/(0.5\rho U_\infty^2)$, where $\tau_{wy}$ is the wall shear stress, computed in the spanwise direction. Its values demonstrate the onset of significant spanwise flows, as a result of the interaction between the wake of the propeller and the hydrofoil.

Results in the near wake of the system at $z/D = 1.5$ are reported in Fig. 7, where all components of the Reynolds stresses are compared between grid resolutions. Profiles are provided along the cross-stream direction $x$ at the spanwise location $y/D = 0.0$. In spite of the complexity of the wake flow, resulting in several local maxima and minima of the cross-stream profiles, comparisons are quite satisfactory, especially for the shear stresses, that almost overlap between resolutions.

It is also worth noting that the contribution of the SGS model was actually found always quite limited. This is demonstrated in Figs. 8 and 9, where the streamwise evolution of the cross-stream profiles is reported for the resolved and modeled Reynolds stresses, respectively in the left and right panels. It should be noted that the right panels refer actually to the deviatoric part of the modeled Reynolds stresses. The two figures deal with the normal and shear stresses, respectively. As demonstrated by the comparison between the left and right panels of Figs. 8 and 9, the modeled stresses are more than three orders of magnitude smaller than the resolved ones, which highlights that the particular choice of the SGS model has a negligible effect on the results, thanks to the resolution of the adopted computational grid.

This result is also reinforced in Fig. 10, dealing with the ratio between eddy and molecular viscosities, keeping always rather small, even on the coarser grid, demonstrating that grid coarsening at downstream coordinates away from the propeller–rudder system is adequate to resolve most of turbulence.

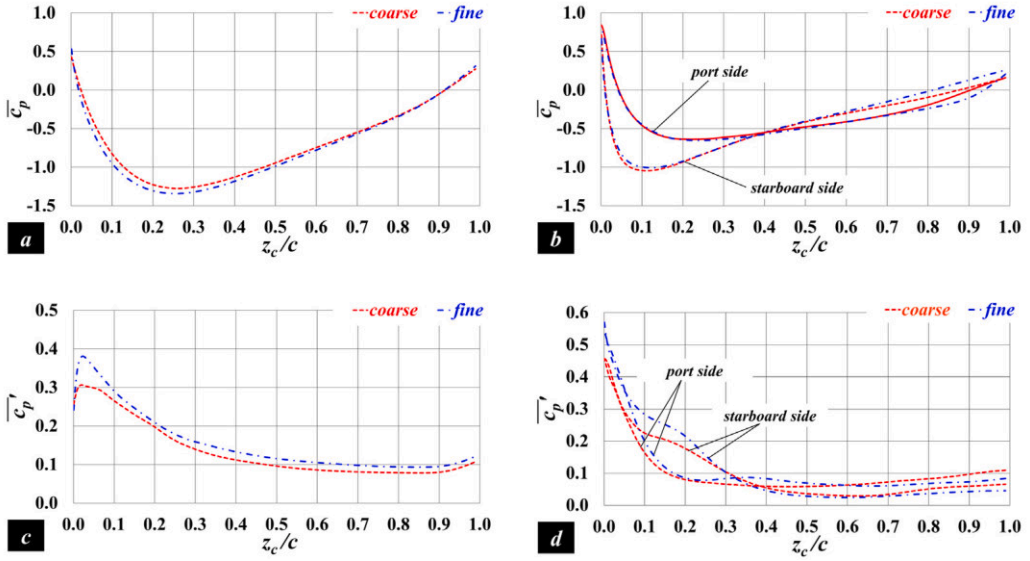


**Fig. 5.** Top panels: time-averaged pressure coefficient on the surface of the infinite hydrofoil at (*a*) $y/D = 0.0$ and (*b*) $y/D = 0.5$. Bottom panels: root-mean-squares in time of the pressure coefficient on the surface of the infinite hydrofoil at (*c*) $y/D = 0.0$ and (*d*) $y/D = 0.5$. Cylindrical grids consisting of 1026 (coarse grid) and 2050 (fine grid) points evenly distributed across the azimuthal direction. Hydrofoil at 0° incidence.

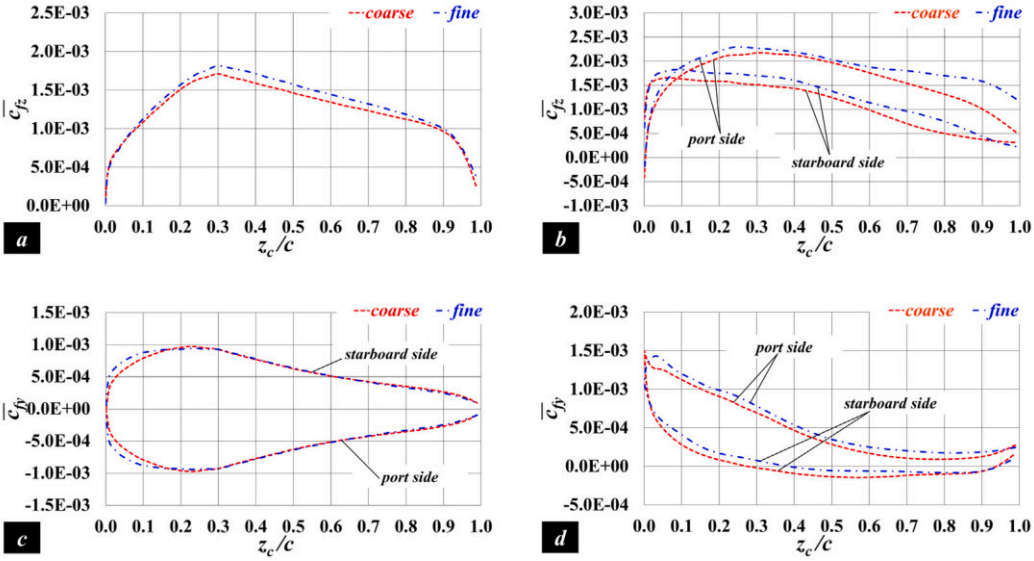


**Fig. 6.** Top panels: time-averaged streamwise skin-friction coefficient on the surface of the infinite hydrofoil at (*a*) $y/D = 0.0$ and (*b*) $y/D = 0.5$. Bottom panels: time-averaged spanwise skin-friction coefficient on the surface of the infinite hydrofoil at (*c*) $y/D = 0.0$ and (*d*) $y/D = 0.5$. Cylindrical grids consisting of 1026 (coarse grid) and 2050 (fine grid) points evenly distributed across the azimuthal direction. Hydrofoil at 0° incidence.

### *4.2. Comparisons across incidence conditions*

In this section detailed comparisons in the near wake of the semi-infinite hydrofoil are reported across incidence conditions. These results will be also exploited to demonstrate the time-convergence of the statistics, computed over 10 revolutions. It is also worth mentioning that the statistics in the wake of the infinite hydrofoil were computed across a much larger sample, consisting of about 40 revolutions. Details dealing with the dependence of the results in the wake of the infinite hydrofoil on the incidence angle are provided in our earlier publications (Posa and Broglia, 2021, 2022a,b,c).

In Fig. 11, cross-stream profiles for the first-order statistics are shown at the spanwise location $y/D = 0.0$, dealing with the streamwise locations $z/D = 2.0$ and $z/D = 3.0$ in the left and right panels, respectively. The dashed lines refer to the final statistics after the whole period $T$ of time-sampling, while the dotted lines to the statistics after half a period, $T/2$. Time-convergence is demonstrated. As expected, the cross-stream velocity, $\overline{u}_x$, shows the shift of the wake from the port side towards the starboard side as the incidence of the hydrofoil grows. In agreement with the findings by earlier works in the literature (Felli and Falchi 2011, Hu et al. 2019, Wang et al. 2019, Felli 2020), the spanwise velocity, $\overline{u}_y$, demonstrates an upward shift of the port side of the wake and an opposite downward shift of the starboard side. It is interesting to notice that the former is diminished by growing incidence angles, while the influence on the latter is milder. The results on the infinite hydrofoil showed an increase of the downward shift of the starboard side of the propeller wake across the hydrofoil at larger incidence angles, but the limited spanwise extent of the hydrofoil has an opposite, balancing effect on the downward flows. The streamwise velocity, $\overline{u}_z$, shows that, while the case ***I*00** is symmetric, as the incidence angle grows this symmetry is broken and the branch of the propeller wake coming

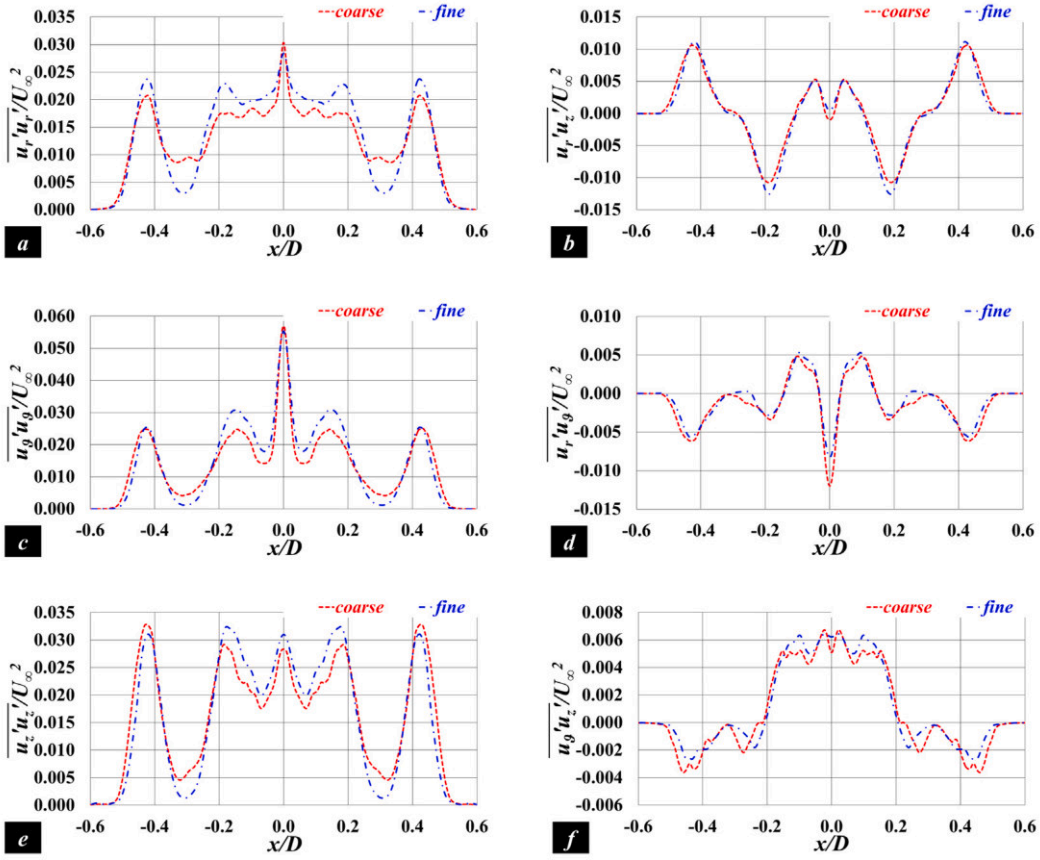


**Fig. 7.** Cross-stream profiles of the resolved Reynolds stresses at the spanwise location $y/D = 0.0$ and the streamwise location $z/D = 1.5$: comparison between simulations on the infinite hydrofoil at 0° incidence on cylindrical grids consisting of 1026 (coarse grid) and 2050 (fine grid) points evenly distributed across the azimuthal direction. Reynolds stresses (*a*) $\overline{u_r'u_r'}$, (*b*) $\overline{u_r'u_z'}$, (*c*) $\overline{u_\vartheta'u_\vartheta'}$, (*d*) $\overline{u_r'u_\vartheta'}$, (*e*) $\overline{u_z'u_z'}$ and (*f*) $\overline{u_\vartheta'u_z'}$.

from the suction side of the hydrofoil is decelerated, in comparison with the one coming from the starboard side. Also the impact of the incidence angle on the pressure minima downstream of the hydrofoil is well distinguishable, resulting in increasingly lower values of pressure, especially on the starboard side.

Results are presented for the turbulent kinetic energy and the shear stresses in Fig. 12, where again time-convergence of the statistics is demonstrated. The profiles of turbulent kinetic energy show that higher values are achieved at larger incidence angles. This is due to the higher turbulence resulting from the adverse streamwise pressure gradient on the suction side of the hydrofoil. However, this influence fades out quickly in the wake, at least at the particular spanwise location, as demonstrated by the comparison between the profiles in the left and right panels of Fig. 12. These results are also consistent with the shear stresses in the near wake. They are not obviously higher at larger angles of incidence at the streamwise location $z/D = 2.0$ and become even a decreasing function of the incidence angle further downstream, which is in agreement with the diminishing gap of levels of turbulent kinetic energy as the flow develops away from the hydrofoil. However, as discussed more in detail later, this result deals with the particular spanwise location and is not general.

Time-convergence of the statistics is also demonstrated in Fig. 13 at the spanwise location $y/D = -0.5$, which is aligned with the bottom tip of the semi-infinite hydrofoil. In contrast with the results seen at $y/D = 0.0$, negative values of cross-stream velocity $\overline{u}_x$ occur, since the pressure gradient between the starboard side and the port side of the hydrofoil results in cross-stream flows from the former towards the latter. It is worth mentioning that this is the case even for the configuration ***I*00**, since the wake of the propeller breaks the symmetry between the two sides of the hydrofoil, generating a cross-stream pressure gradient between them. The profiles of Fig. 13*a*, *b* point to a strong dependence of the cross-stream velocity on the incidence angle of the hydrofoil, characterized by an especially large negative peak for ***I*15**. Also the profiles of spanwise velocity in Fig. 13*c*, *d* highlight the importance of the end effects: the negative peaks on the bottom side are lower than the positive ones on the top side (not shown here), due to the cross-stream flows originating from the starboard side towards the port side at the bottom end of the hydrofoil. For the streamwise velocity the most obvious effect of the incidence angle is the gradual shift from the port towards the starboard side. The behavior of the pressure coefficient is more interesting, since characterized by the onset of a significant negative peak, associated with the tip vortex shed from the bottom end of the hydrofoil, due to the vorticity roll-up from its starboard side towards its port side. This peak is also a very strong function of the orientation of the hydrofoil.

Second-order statistics are illustrated in Fig. 14. The peaks of turbulent kinetic energy are associated with the tip vortices generated by the semi-infinite hydrofoil and are a growing function of the incidence angle, as shown in Fig. 14*a*. They are shifted on the side of negative cross-stream coordinates, since they originate from the cross-stream flows oriented from the starboard side towards the port side of the hydrofoil. This displacement of the highest values of turbulent kinetic energy towards the port side is still distinguishable in Fig. 14*b*, in spite of the orientation of the hydrofoil and the displacement of the wake flow of the propeller–rudder system from the port side towards the starboard side. At this spanwise location the shear stresses, with the exception of $\overline{u_\vartheta'u_z'}$, display a more obvious dependence on the incidence angle, in comparison with the results seen at $y/D = 0.0$. In Fig. 14, they show only a small dependence on the size of the time sample.

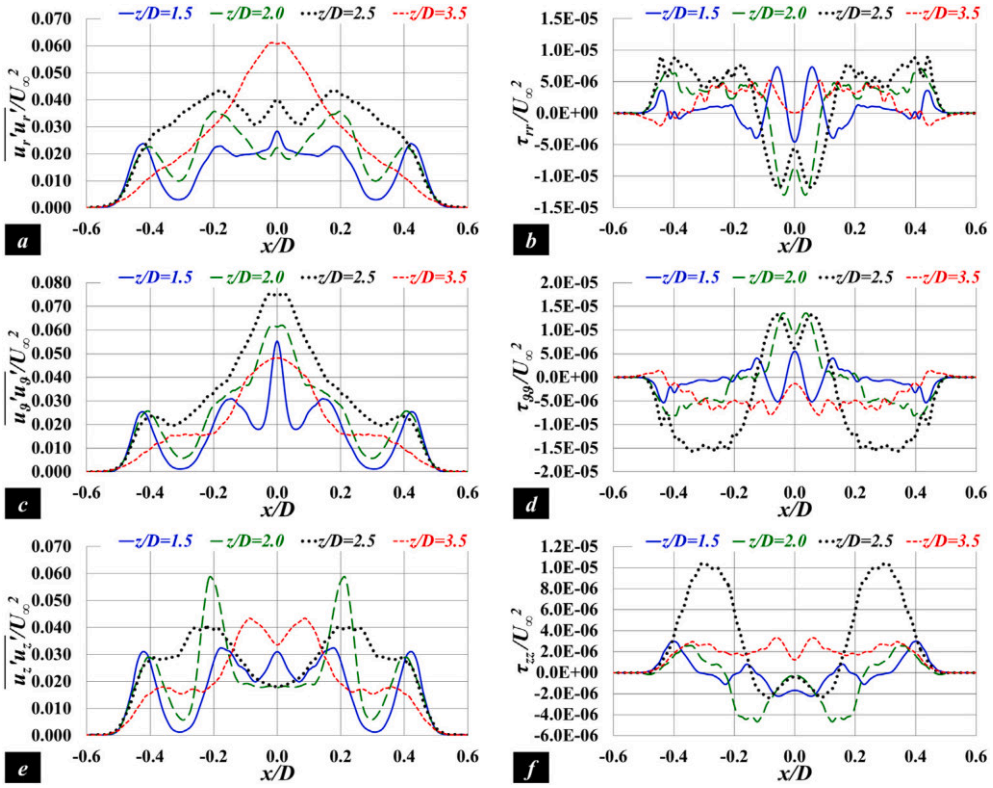


**Fig. 8.** Cross-stream profiles of the resolved (left panels) and modeled (right panels) normal Reynolds stresses at the spanwise location $y/D = 0.0$ and the streamwise locations $z/D = 1.5$, $z/D = 2.0$, $z/D = 2.5$ and $z/D = 3.5$ downstream of the infinite hydrofoil at 0° incidence on the cylindrical grid consisting of 2050 (fine grid) points evenly distributed across the azimuthal direction: (*a*) $\overline{u_r'u_r'}$, (*b*) $\tau_{rr}$, (*c*) $\overline{u_\vartheta'u_\vartheta'}$, (*d*) $\tau_{\vartheta\vartheta}$, (*e*) $\overline{u_z'u_z'}$ and (*f*) $\tau_{zz}$.

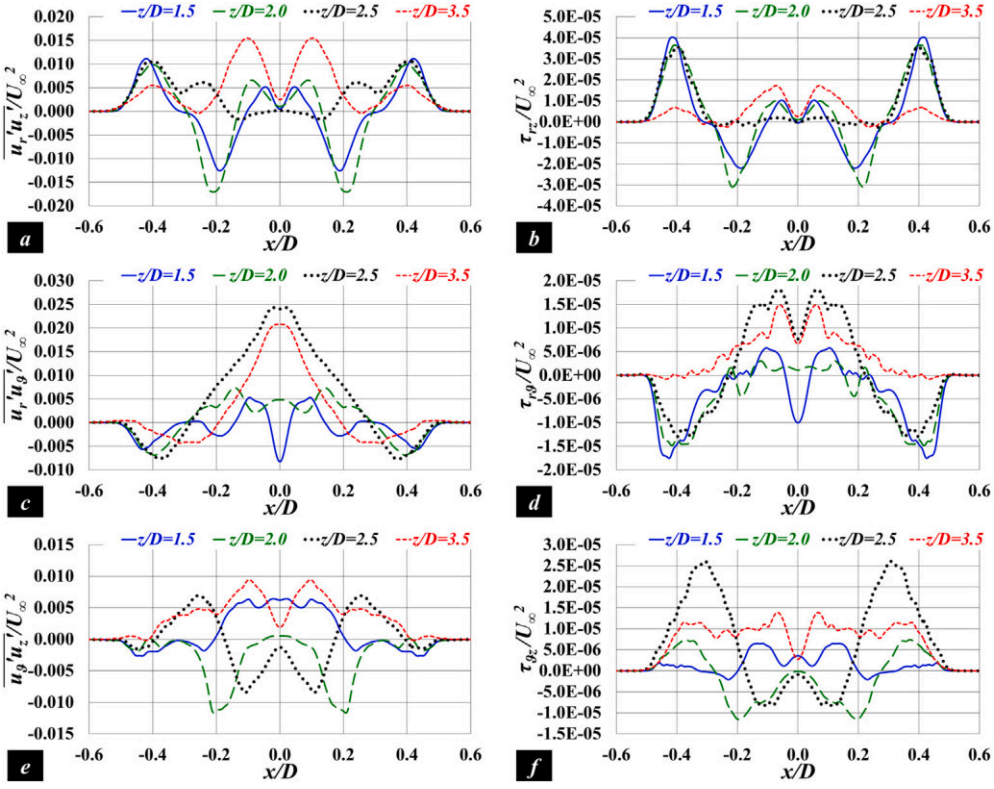


**Fig. 9.** Cross-stream profiles of the resolved (left panels) and modeled (right panels) shear Reynolds stresses at the spanwise location $y/D = 0.0$ and the streamwise locations $z/D = 1.5$, $z/D = 2.0$, $z/D = 2.5$ and $z/D = 3.5$ downstream of the infinite hydrofoil at 0° incidence on the cylindrical grid consisting of 2050 (fine grid) points evenly distributed across the azimuthal direction: (*a*) $\overline{u_r'u_z'}$, (*b*) $\tau_{rz}$, (*c*) $\overline{u_r'u_\vartheta'}$, (*d*) $\tau_{r\vartheta}$, (*e*) $\overline{u_\vartheta'u_z'}$ and (*f*) $\tau_{\vartheta z}$.

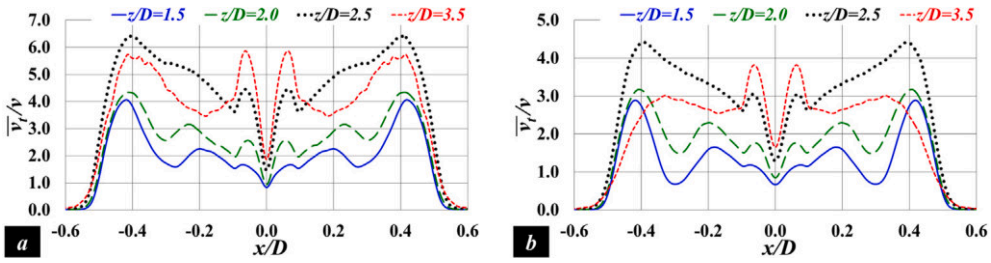


**Fig. 10.** Time-averaged ratio between the eddy and molecular viscosities at the spanwise location $y/D = 0.0$ and the streamwise locations $z/D = 1.5$, $z/D = 2.0$, $z/D = 2.5$ and $z/D = 3.5$ downstream of the infinite hydrofoil at 0° incidence: results on the cylindrical grids consisting of (*a*) 1026 (coarse grid) and (*b*) 2050 (fine grid) points evenly distributed across the azimuthal direction.

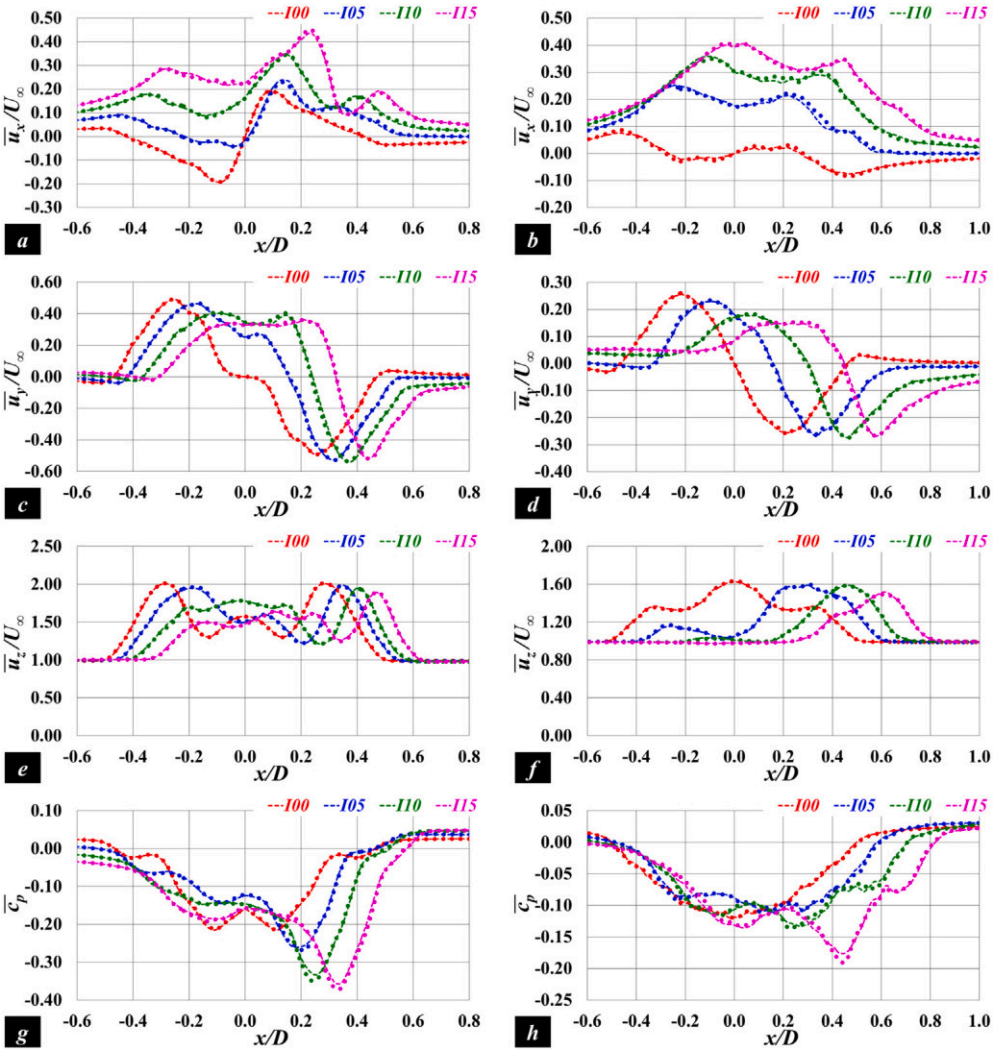


**Fig. 11.** Cross-stream profiles of the time-averaged (*a*, *b*) cross-stream velocity, (*c*, *d*) spanwise velocity, (*e*, *f*) streamwise velocity and (*g*, *h*) pressure coefficient at the spanwise location $y/D = 0.0$ and the streamwise locations $z/D = 2.0$ (left panels) and $z/D = 3.0$ (right panels) downstream of the semi-infinite hydrofoil. Dashed lines for the statistics across the whole period of time-sampling, dotted lines for the statistics across half a period.

### *4.3. Comparison of the SPLs between infinite and semi-infinite hydrofoils*

#### *4.3.1. Hydrophones at r/D=1.5 and z/D=1.0*

Comparisons between infinite and semi-infinite hydrofoils are reported in Fig. 15, where the $SPLs$ are provided at the 72 hydrophones of radial coordinate $r/D = 1.5$ and streamwise coordinate $z/D = 1.0$. Values were averaged across the azimuthal direction. The four panels deal with the four simulated incidence angles of the two hydrofoils. Also open-water results of the isolated propeller are reported. In all cases with downstream hydrofoil, the increase, compared to the open-water configuration, is evident. The $SPLs$ relative to the infinite hydrofoil are usually higher, compared to the case of the semi-infinite one. This result is mainly attributable to the non-linear terms (Fig. 16), which are higher in the former case across all frequencies and orientations, due to the growth of the boundary layer in the bottom region of the hydrofoil, especially at large incidence angles, for which higher $SPLs$ are achieved.

The complexity of the flow physics is illustrated in Fig. 17, where isosurfaces from phase-averaged statistics are shown on the port side, using the $Q$-criterion by Jeong and Hussain (1995). They are colored

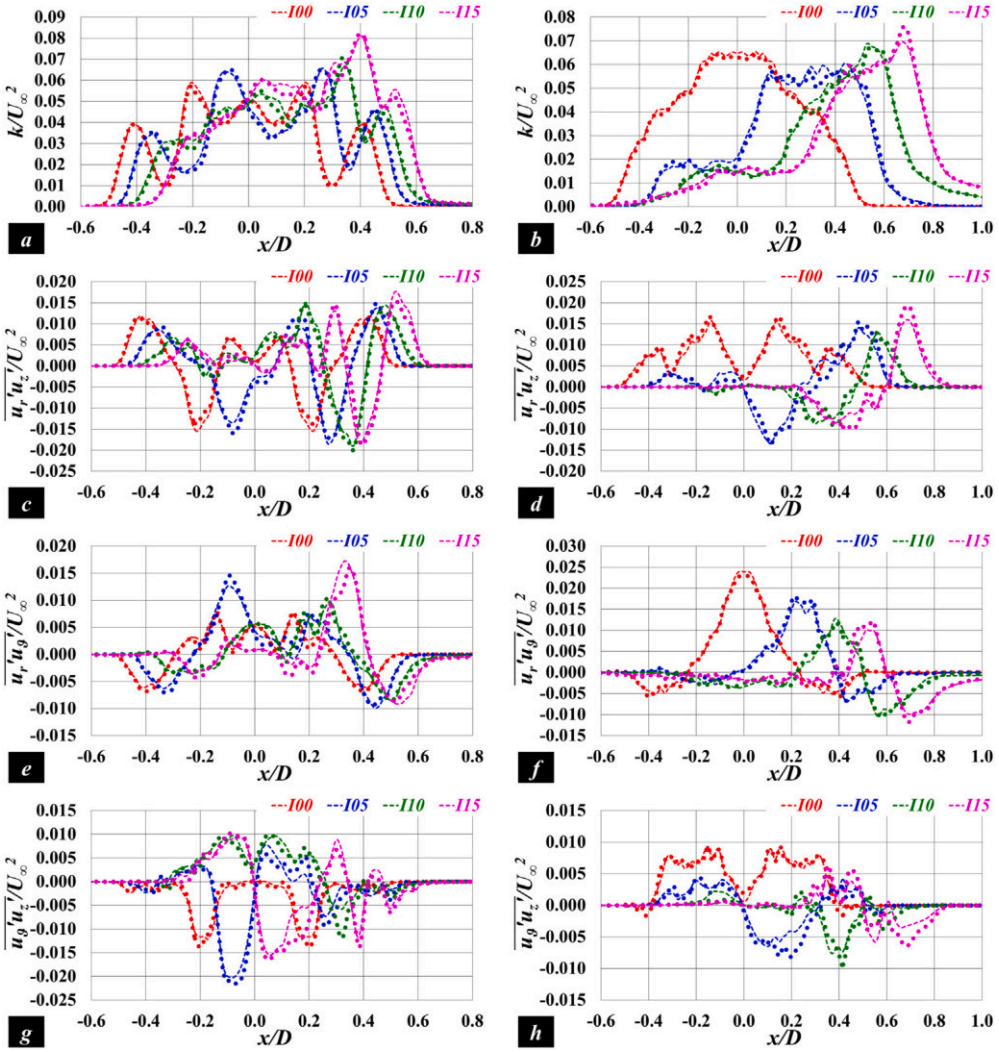


**Fig. 12.** Cross-stream profiles of (*a*, *b*) turbulent kinetic energy and shear stresses (*c*, *d*) $\overline{u_r'u_z'}$, (*e*, *f*) $\overline{u_r'u_\theta'}$ and (*g*, *h*) $\overline{u_\theta'u_z'}$ at the spanwise location $y/D = 0.0$ and the streamwise locations $z/D = 2.0$ (left panels) and $z/D = 3.0$ (right panels) downstream of the semi-infinite hydrofoil. Dashed lines for the statistics across the whole period of time-sampling, dotted lines for the statistics across half a period.

by using the azimuthal vorticity. The left side deals with the case of the infinite hydrofoil, the right side with the semi-infinite one. The latter are more noisy than the former, due to the smaller size of the statistical sample. Note that for the cases with the hydrofoil at incidence its port side is the suction side. In agreement with the results in the literature (Felli and Falchi 2011, Hu et al. 2019, Wang et al. 2019, Felli 2020) the interaction between the propeller wake and the hydrofoil results, even in the case at 0° incidence, in an upward shift of the former. This affects both the upper and lower branches of the tip vortices, whose axial velocities are directed respectively towards and away from the surface of the hydrofoil. This behavior is not modified between the left and right panels of Fig. 17, since the propeller wake is deflected upwards, where the two geometries are identical. The major difference between them is instead the onset of two tip vortices from the bottom end of the semi-infinite hydrofoil. Increasing incidence angles have also similar effects on the flow physics: the propeller wake experiences a contraction, since the deflection of the upper tip vortices is diminished, while that of the lower tip vortices is reinforced. As expected, the tip vortices shed from the bottom end of the semi-infinite hydrofoil become more intense as its incidence angle grows, due to the increasing pressure gradient and cross-stream flow between its port and starboard sides.

On the starboard side the differences in the wake development between hydrofoil geometries become more evident, as illustrated in Fig. 18, since the propeller wake experiences there a downward deflection, affecting both the upper and lower branches of the tip vortices, whose axial velocity on this side is directed away and towards the surface of the hydrofoil, respectively. Also in this case the flow physics is in close agreement with earlier studies on the subject. The effect of the incidence angle consists in an expansion of the propeller wake, since the downward shift of the upper vortices is diminished and that of the lower vortices is reinforced. Both downward shift and expansion, coming from the interaction of the propeller wake with the surface of the hydrofoil, are diminished by its finite extent, as demonstrated by the comparison between the left and right panels of Fig. 18. Actually, the right panels of Fig. 18 show that the downward shift of the propeller wake is replaced by cross-stream flows from the starboard side towards the port side of the hydrofoil, as demonstrated by the tip vortices from the propeller, moving to the opposite side, even in the case at 0° incidence: as discussed above, the propeller wake introduces a pressure gradient between the two sides of the hydrofoil, even in the case it is aligned with the free-stream.

In Fig. 19, contours of time-averaged streamwise velocity are reported at the location $z/D = 1.0$, including isolines of $\overline{u}_z = 0$, which are useful to isolate regions of separated flow. In the top panels of Fig. 19, dealing with the infinite hydrofoil, it is clear that the boundary layer experiences a significant growth, especially on its port-bottom side. The

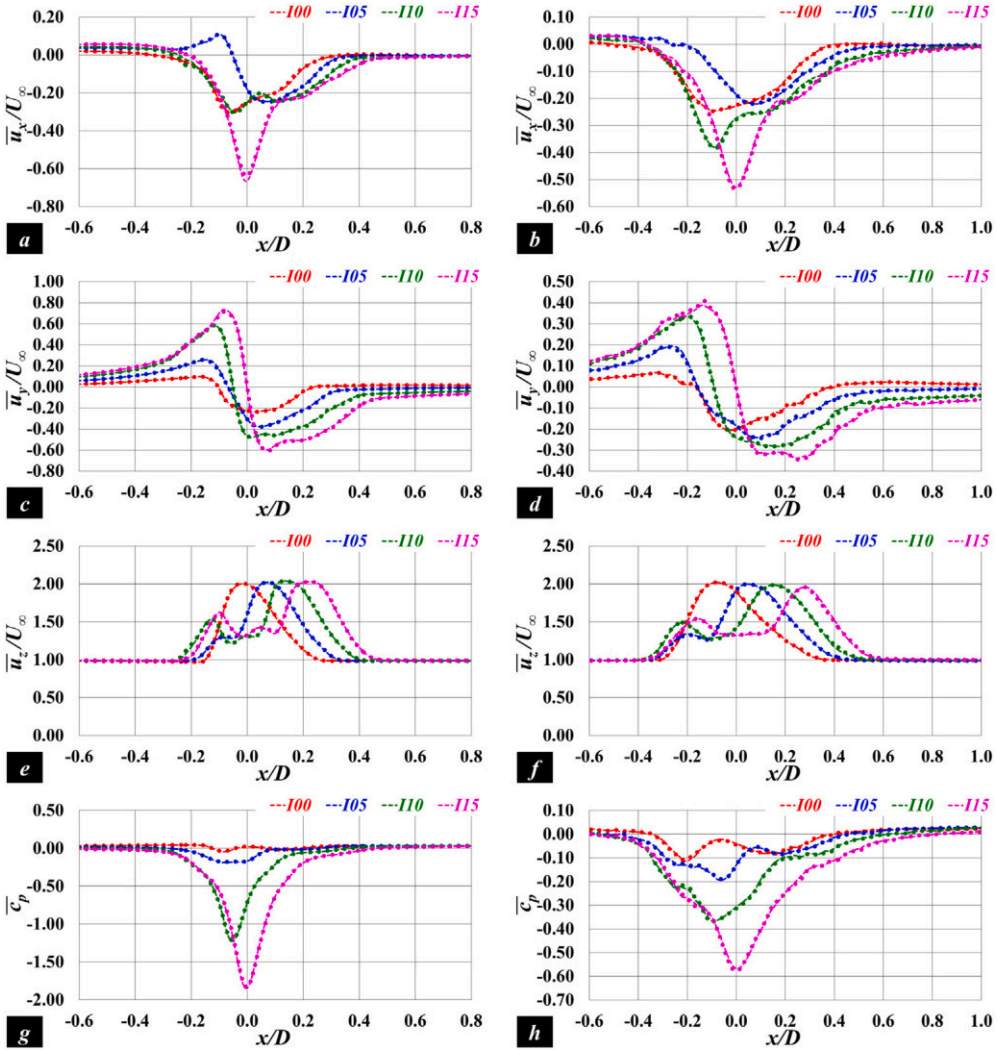


**Fig. 13.** Cross-stream profiles of the time-averaged (*a*, *b*) cross-stream velocity, (*c*, *d*) spanwise velocity, (*e*, *f*) streamwise velocity and (*g*, *h*) pressure coefficient at the spanwise location $y/D = -0.5$ and the streamwise locations $z/D = 2.0$ (left panels) and $z/D = 3.0$ (right panels) downstream of the semi-infinite hydrofoil. Dashed lines for the statistics across the whole period of time-sampling, dotted lines for the statistics across half a period.

port/suction side is more affected, due to the decelerating effect by the adverse streamwise pressure gradient when the hydrofoil works at incidence. In addition, the growth of the boundary layer is faster on the bottom side, due to the spanwise shift of the propeller wake. The flow coming from the propeller has a beneficial effect, energizing the boundary layer on the hydrofoil and opposing its instability and separation. However, as illustrated above, the interaction of the propeller wake with the surface of the hydrofoil results in its upward shift on the port side. As a consequence, the boundary layer on the bottom side of the hydrofoil is less energized by the propeller wake than the top side, growing and approaching separation at a faster rate.

In the bottom panels of Fig. 19 the flow is dramatically modified. It should be noted that in the case of the infinite hydrofoil the onset of separation occurs at outer spanwise coordinates, propagating towards the inner ones, that is from negative $y$ coordinates towards the wake axis. In Fig. 19*d* the wide region of backflow is identified by means of the isoline of zero streamwise velocity in the bottom region of the port side of the hydrofoil. Actually, also at smaller incidence angles the boundary layer is decelerating and approaching separation. These phenomena are missing on the bottom side of the semi-infinite hydrofoil. In addition, due to the pressure gradient between the two sides of the hydrofoil, momentum moves from the starboard side towards the port side of the semi-infinite geometry, energizing the flow on the latter. As a result, the separation phenomena occurring at large incidence angles on the side of negative $y$ coordinates in the top panels of Fig. 19 are missing in the bottom ones.

In Fig. 20, contours of mean squares of the fluctuations in time of streamwise velocity, $\overline{u_z' u_z'}$, are reported at the location $z/D = 1.0$. In Fig. 20*a*, dealing with the infinite hydrofoil at no incidence, the major areas of turbulent fluctuations are the hub and tip vortices from the propeller, whose signature is well distinguishable. As the incidence angle grows, from the left to the right panels, the destabilizing effect by the adverse pressure gradient causes a rise of turbulence levels in the boundary layer on the port/suction side of the hydrofoil. This effect is actually more evident at outer spanwise coordinates, since at the inner ones the acceleration produced by the propeller wake is beneficial in stabilizing the boundary layer. For increasing incidence angles, the instability of the boundary layer moves from outer to inner coordinates. This is due to both the increasing adverse pressure gradient and the spanwise contraction of the branch of the propeller wake on the suction side of the hydrofoil. Eventually, as shown in Fig. 20*d*, separation phenomena cause a displacement of the peak of turbulent fluctuations away from the wall.

The bottom panels of Fig. 20, dealing with the semi-infinite approximation, confirm that the physics of the flow is substantially modified, at least on the side of negative $y$ coordinates, which are actually those

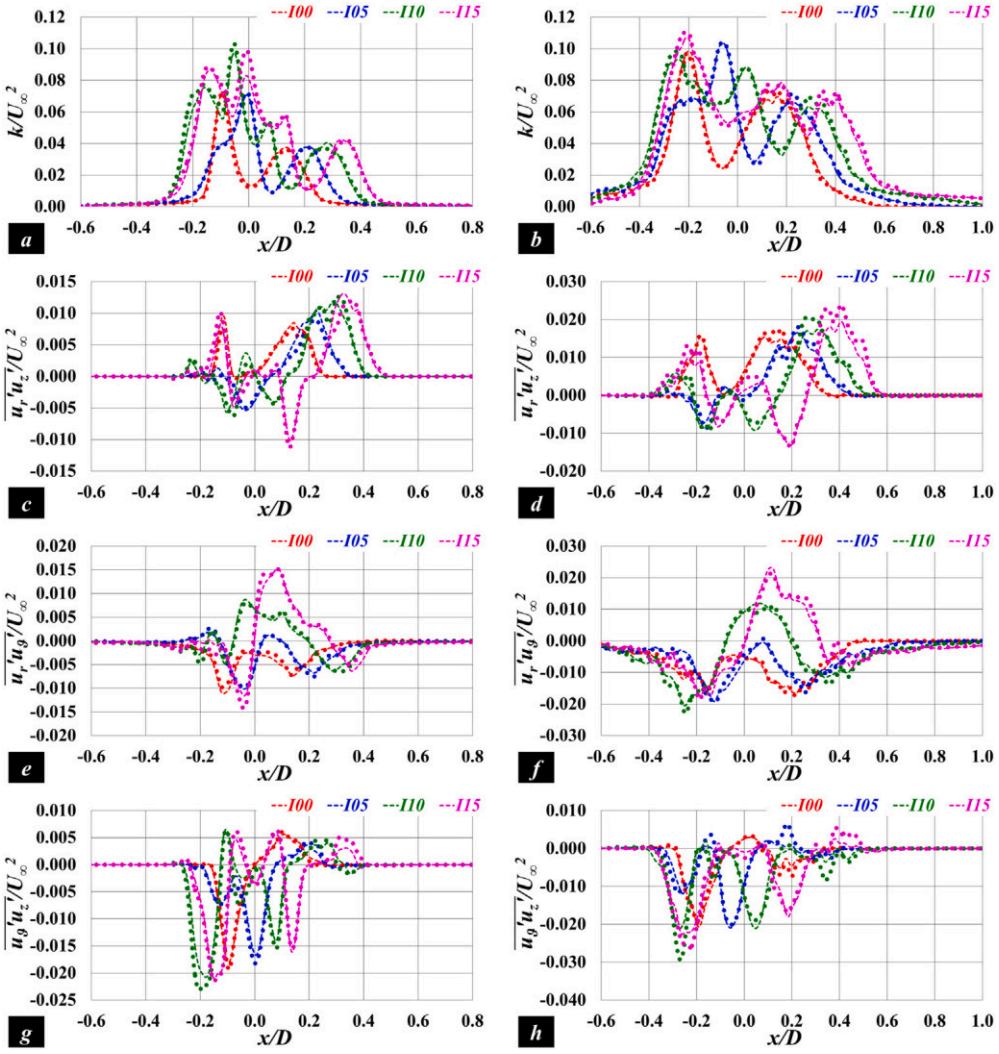


**Fig. 14.** Cross-stream profiles of (*a*, *b*) turbulent kinetic energy and shear stresses (*c*, *d*) $\overline{u_r' u_z'}$, (*e*, *f*) $\overline{u_r' u_\vartheta'}$ and (*g*, *h*) $\overline{u_\vartheta' u_z'}$ at the spanwise location $y/D = -0.5$ and the streamwise locations $z/D = 2.0$ (left panels) and $z/D = 3.0$ (right panels) downstream of the semi-infinite hydrofoil. Dashed lines for the statistics across the whole period of time-sampling, dotted lines for the statistics across half a period.

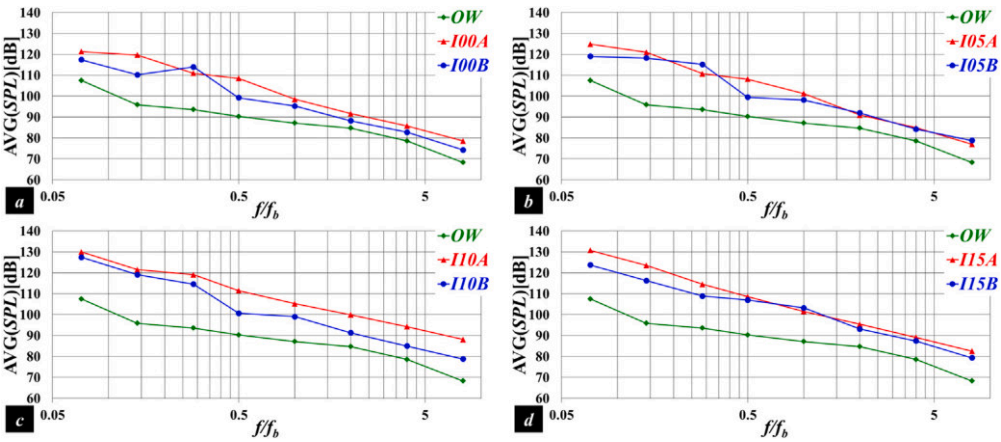


**Fig. 15.** Azimuthal averages of the $SPLs$ in third-octave bands at hydrophones of radial and axial coordinates $r/D = 1.5$ and $z/D = 1.0$, respectively: comparison between the simulations on the (*A*) infinite and (*B*) semi-infinite hydrofoils, including values in (*OW*) open-water conditions. Cases (*a*) ***I*00**, (*b*) ***I*05**, (*c*) ***I*10** and (*d*) ***I*15**.

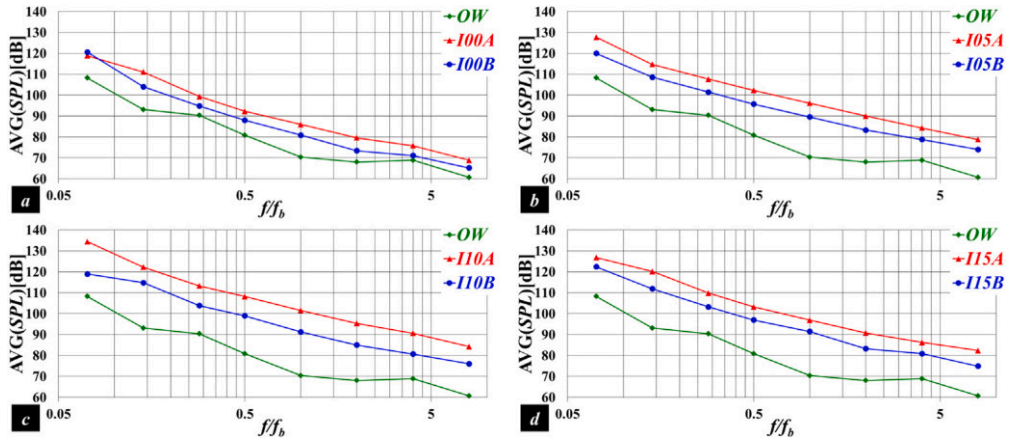


**Fig. 16.** Azimuthal averages of the non-linear component of the $SPLs$ in third-octave bands at hydrophones of radial and axial coordinates $r/D = 1.5$ and $z/D = 1.0$, respectively: comparison between the simulations on the ($A$) infinite and ($B$) semi-infinite hydrofoils, including values in ($OW$) open-water conditions. Cases ($a$) ***I*00**, ($b$) ***I*05**, ($c$) ***I*10** and ($d$) ***I*15**.

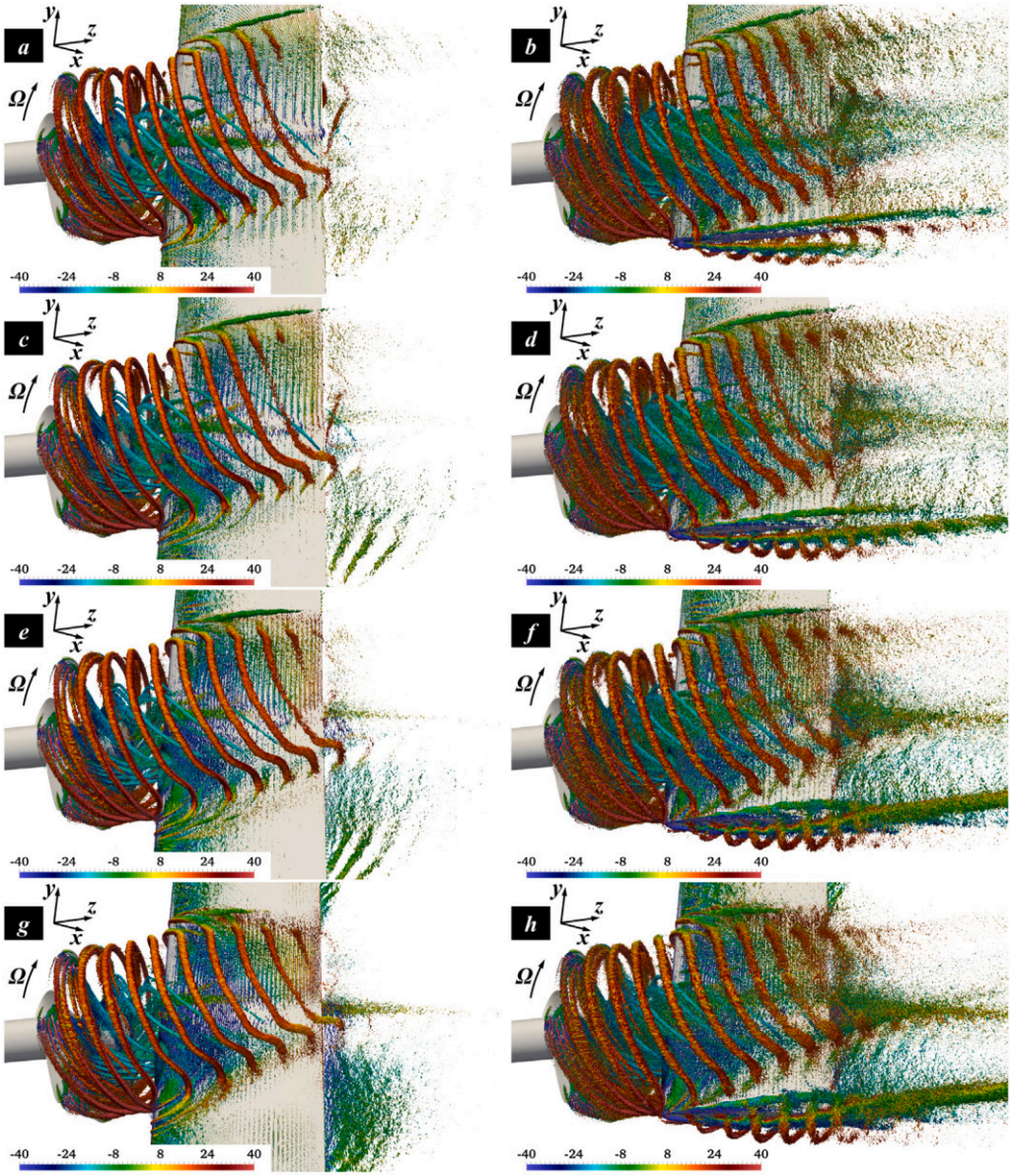


**Fig. 17.** Visualization of the coherent structures on the port side through the $Q$-criterion ($QD^2/U_\infty^2 = 100$) from phase-averaged statistics. Colors for the azimuthal vorticity, scaled by $U_\infty/D$. Configurations ($a$, $b$) ***I*00**, ($c$, $d$) ***I*05**, ($e$, $f$) ***I*10** and ($g$, $h$) ***I*15**. Left and right panels for the infinite and semi-infinite hydrofoils, respectively.

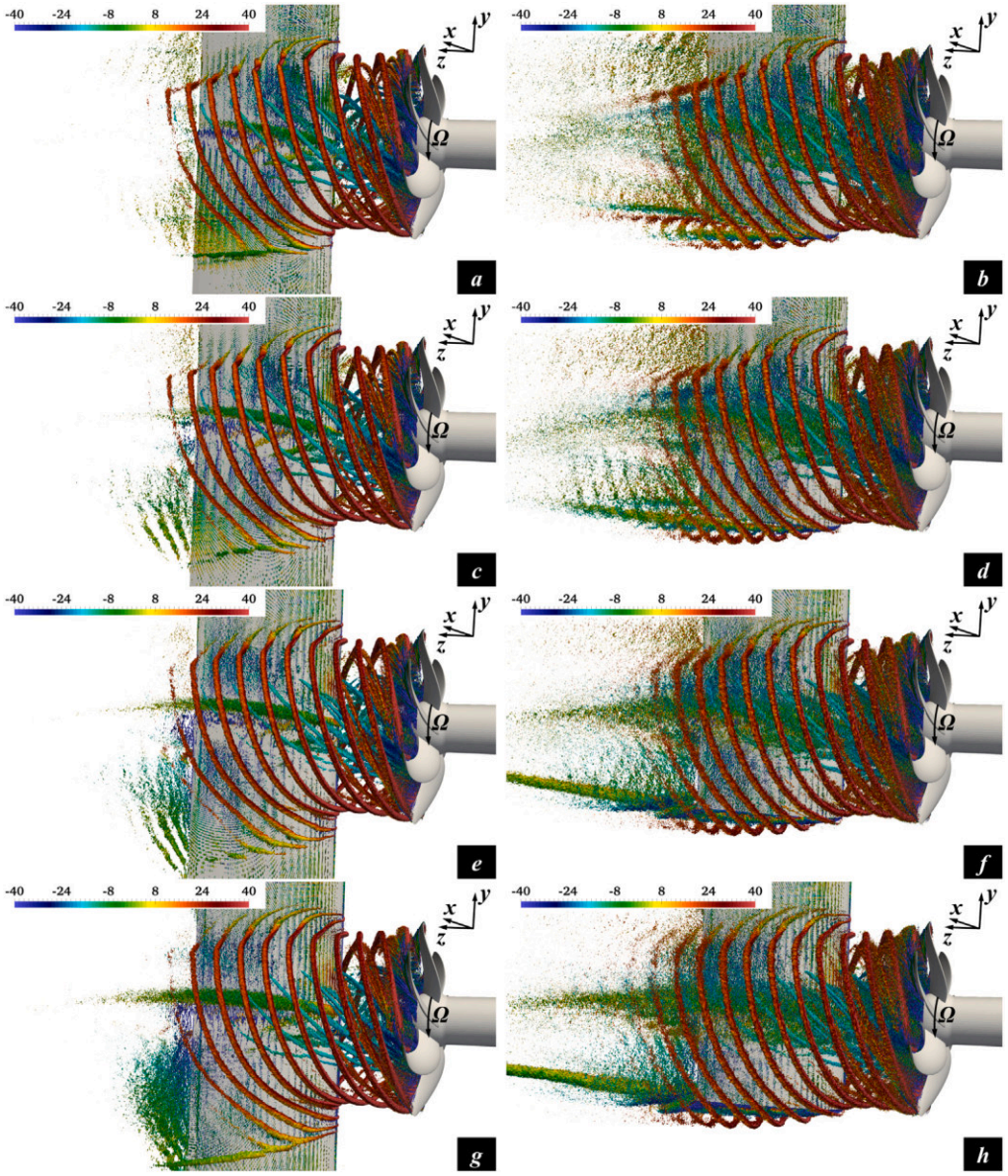


**Fig. 18.** Visualization of the coherent structures on the starboard side through the $Q$-criterion ($QD^2/U_\infty^2 = 100$) from phase-averaged statistics. Colors for the azimuthal vorticity, scaled by $U_\infty/D$. Configurations ($a$, $b$) ***I*00**, ($c$, $d$) ***I*05**, ($e$, $f$) ***I*10** and ($g$, $h$) ***I*15**. Left and right panels for the infinite and semi-infinite hydrofoils, respectively.

experiencing the most significant separation phenomena for the infinite hydrofoil. Turbulence levels are dramatically reduced, although an additional location of large turbulence is produced at the core of the vortex arising at the tip of the hydrofoil, as a result of the pressure gradient between its starboard and port sides. This turbulence peak is a growing function of the incidence angle. This overall reduction of the turbulence levels is in line with the lower values of non-linear sound for the case of the semi-infinite hydrofoil, in comparison with the infinite one.

In this region of the domain ($r/D = 1.5$ and $z/D = 1.0$) the linear component of the $SPLs$ coming from the surface of the hydrofoil was found comparable with the non-linear one. However, it was verified that the major source of the higher $SPLs$ for the case of the infinite hydrofoil, compared to the semi-infinite one, is usually the non-linear sound, whose levels are consistently higher in the former case, as shown above in Fig. 16. Actually, Fig. 21, dealing with the sound from the surface of the hydrofoil, shows also some differences between the cases of the infinite and semi-infinite spanwise extents. However, although the $SPLs$ in Fig. 21 are also usually higher in the former case, several exceptions are distinguishable across frequencies and incidence angles. For limitation of space a similar comparison is not reported for the linear terms attributable to the surface of the propeller, since they are lower, as the propeller in the present setup is operating within a uniform flow. However, as expected, for them the deviations between the two approximations of the hydrofoil geometry were found practically negligible.

#### 4.3.2. Hydrophones at r/D=1.5 and z/D=4.0

Fig. 22 deals with results for hydrophones at $r/D = 1.5$ and $z/D = 4.0$, to shed light on the downstream development of the acoustic signature. It is interesting to see that the differences between cases of infinite and semi-infinite hydrofoils become more homogeneous across frequencies. In addition, while at no incidence they are practically negligible, they grow at larger incidence angles. This behavior is dominated by the non-linear terms of the acoustic signature, due to the instability phenomena affecting the wake: the results in Fig. 23 show indeed comparisons across the components of the $SPLs$. It is clear that in all cases the non-linear terms are much higher than the linear ones:

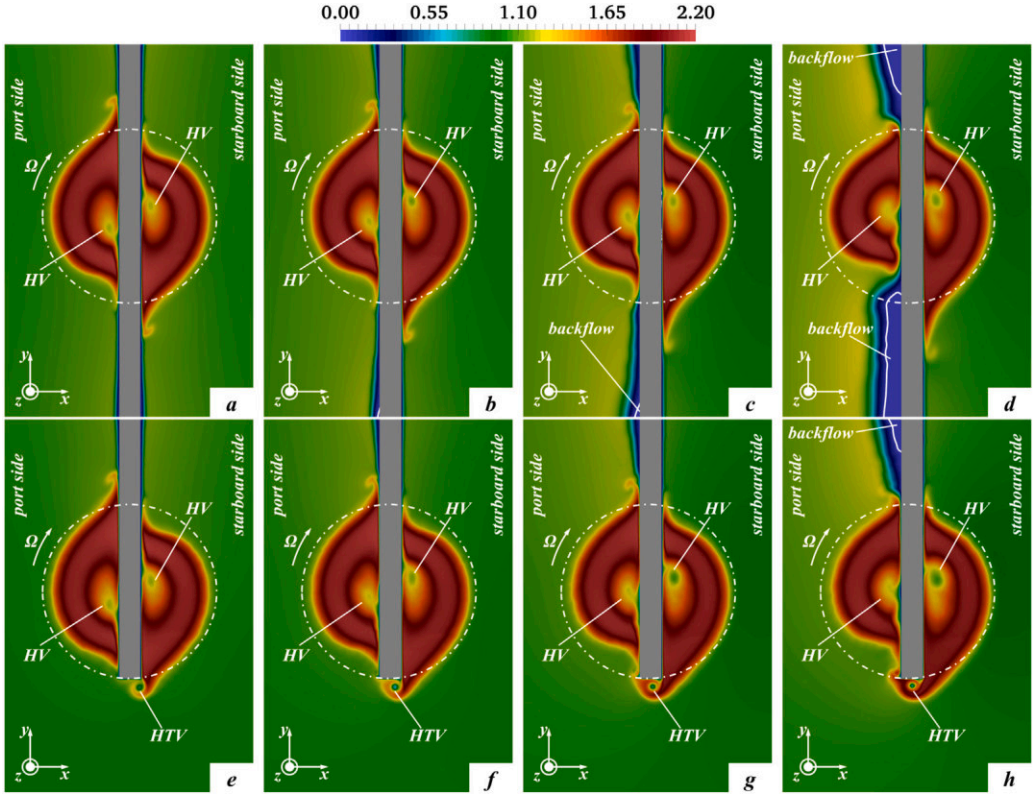


**Fig. 19.** Contours of time-averaged streamwise velocity, scaled by $U_\infty$, at $z/D = 1.0$. Isolines for $\overline{u}_z = 0$. Comparison between the simulations on the (top panels) infinite and (bottom panels) semi-infinite hydrofoils. Cases (*a*, *e*) ***I00***, (*b*, *f*) ***I05***, (*c*, *g*) ***I10*** and (*d*, *h*) ***I15***. ***HV***: hub vortex from the propeller. ***HTV***: tip vortex from the hydrofoil. Dotted-dashed line encompassing the projection of the area swept by the propeller blades. Gray area for the section of the hydrofoil at the particular streamwise location.

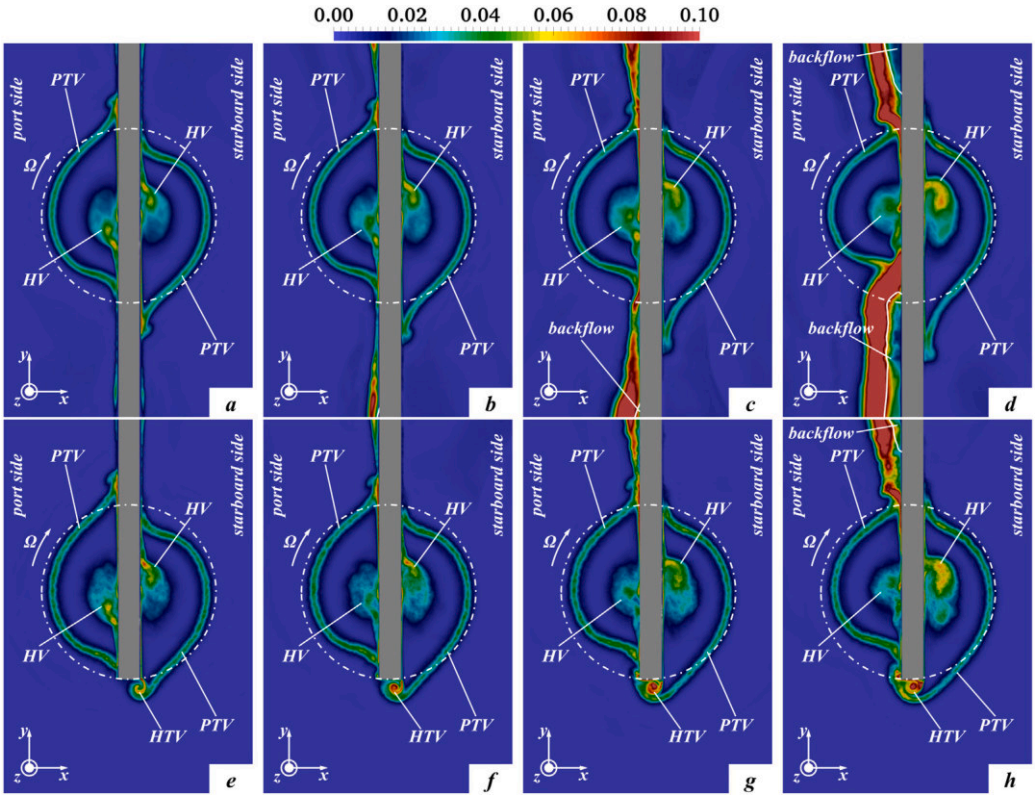


**Fig. 20.** Contours of the mean squares of the time-fluctuations of streamwise velocity, $\overline{u'_z u'_z}$, scaled by $U_\infty^2$, at $z/D = 1.0$. Isolines for $\overline{u}_z = 0$. Comparison between the simulations on the (top panels) infinite and (bottom panels) semi-infinite hydrofoils. Cases (*a*, *e*) ***I00***, (*b*, *f*) ***I05***, (*c*, *g*) ***I10*** and (*d*, *h*) ***I15***. ***PTV***: tip vortices from the propeller. ***HV***: hub vortex from the propeller. ***HTV***: tip vortex from the hydrofoil. Dot-dashed line encompassing the projection of the area swept by the propeller blades. Gray area for the section of the hydrofoil at the particular streamwise location.

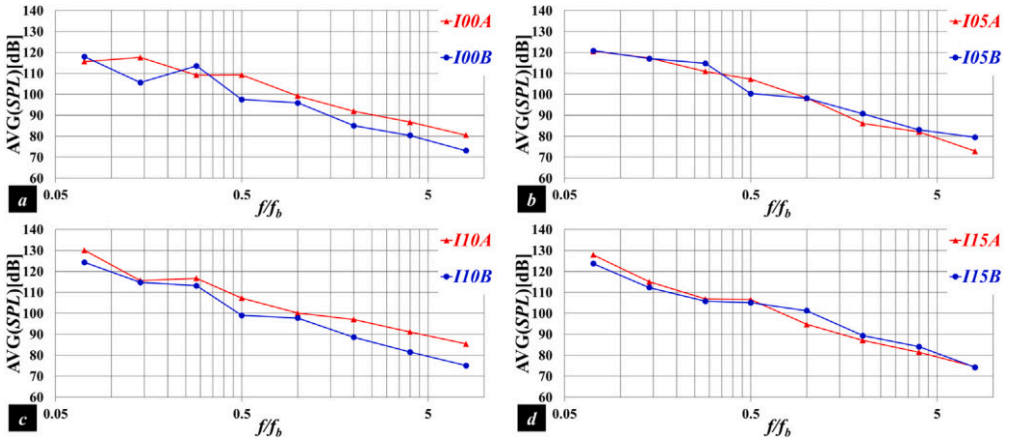


**Fig. 21.** Azimuthal averages of the linear component of the $SPLs$ in third-octave bands from the surface of the hydrofoil at hydrophones of radial and axial coordinates $r/D = 1.5$ and $z/D = 1.0$, respectively: comparison between the simulations on the $(A)$ infinite and $(B)$ semi-infinite hydrofoils. Cases $(a)$ ***I*00**, $(b)$ ***I*05**, $(c)$ ***I*10** and $(d)$ ***I*15**.

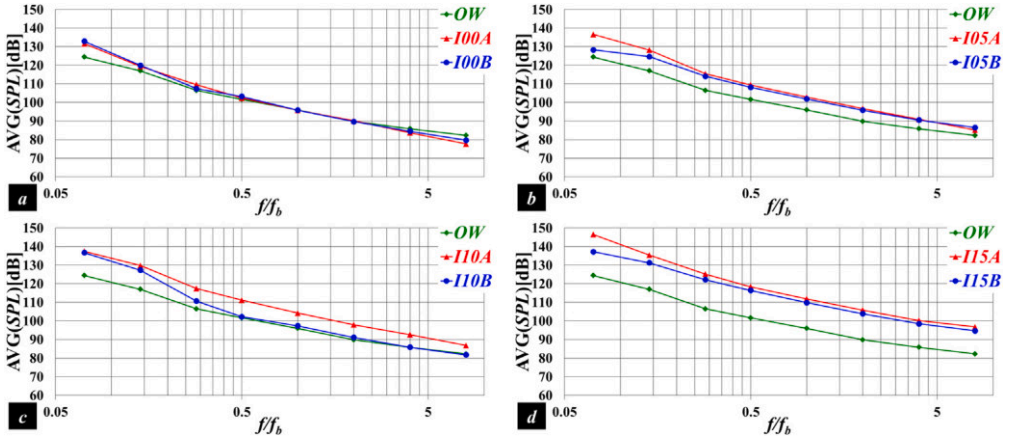


**Fig. 22.** Azimuthal averages of the $SPLs$ in third-octave bands at hydrophones of radial and axial coordinates $r/D = 1.5$ and $z/D = 4.0$, respectively: comparison between the simulations on the $(A)$ infinite and $(B)$ semi-infinite hydrofoils, including values in $(OW)$ open-water conditions. Cases $(a)$ ***I*00**, $(b)$ ***I*05**, $(c)$ ***I*10** and $(d)$ ***I*15**.

while the former are rising in the streamwise direction, as a result of the growing instabilities of the wake system, the latter are declining, due to the increasing distance from their sources.

The growing trend of the turbulent fluctuations downstream of the hydrofoil is demonstrated in Fig. 24. Their integrals over cross-sections of radial extent equal to $1.2D$ are shown, computed as below:

$$I\left[\overline{u_i' u_j'}\right] = \int_{\vartheta=0}^{\vartheta=2\pi} \int_{r=0}^{r=1.2D} \overline{u_i' u_j'}\, dr\, d\vartheta. \tag{14}$$

In the left and right panels of Fig. 24 the cases of the infinite and semi-infinite hydrofoils are considered, respectively, for increasing incidence angles from top to bottom. The streamwise evolution in the near wake is growing, reinforcing the importance of the quadrupole component of sound. $I[|\overline{u_r' u_\vartheta'}|]$ is the fastest to achieve its peak, a few diameters downstream of the trailing edge of the hydrofoil. Turbulent kinetic energy peaks further downstream. $I[|\overline{u_r' u_z'}|]$ and $I[|\overline{u_\vartheta' u_z'}|]$ are the slowest to reach their highest values. This behavior is shared across cases of incidence and spanwise extent of the hydrofoil, with the exception of the configuration ***I*15** for the infinite hydrofoil (Fig. 24*g*). In that case the flow physics is substantially modified, because of massive separation phenomena on the suction side of the hydrofoil. Therefore, while $I[|\overline{u_r' u_\vartheta'}|]$, $I[|\overline{u_r' u_z'}|]$ and $I[k]$ keep a rising streamwise evolution across the near wake of the system, $I[|\overline{u_\vartheta' u_z'}|]$ achieves its peak within the separated boundary layer, decreasing monotonically downstream of the hydrofoil. In contrast, although for both hydrofoil geometries the turbulent stresses in the near wake are a growing function of their incidence angle, in the case of the semi-infinite hydrofoil their streamwise evolution does not experience substantial qualitative changes across the four simulated configurations.

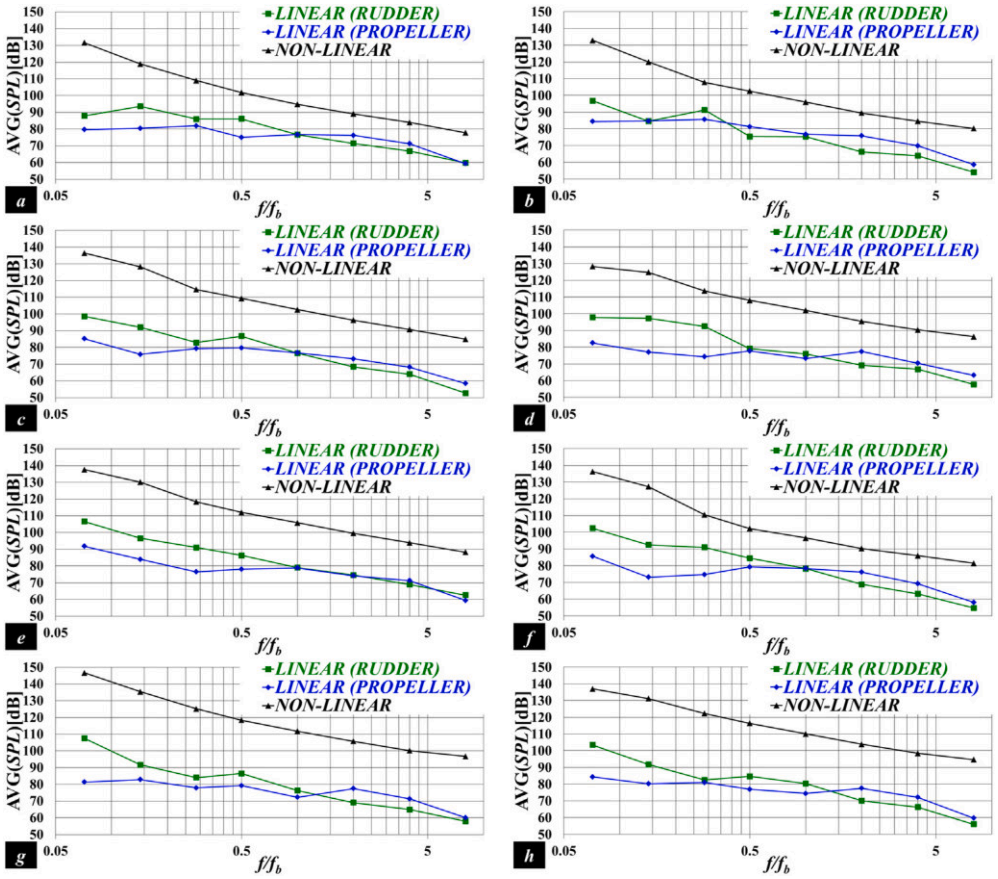


**Fig. 23.** Azimuthal averages of the $SPLs$ in third-octave bands at hydrophones of radial and axial coordinates $r/D = 1.5$ and $z/D = 4.0$, respectively: comparison across components of $SPLs$ between the simulations on the (left panels) infinite and (right panels) semi-infinite hydrofoils. Cases (*a*, *b*) ***I*00**, (*c*, *d*) ***I*05**, (*e*, *f*) ***I*10** and (*g*, *h*) ***I*15**.

The interpretation of the results above is straightforward. While at no incidence the wake development is similar downstream of the infinite and semi-infinite hydrofoils, this is no longer the case at large incidence angles. This is demonstrated by the comparison between Figs. 25 and 26, showing contours of time-averaged streamwise velocity at $z/D = 4.0$ downstream of the infinite and semi-infinite hydrofoils, respectively. While at no incidence (Fig. 25*a* and Fig. 26*a*) the signature of the propeller–rudder system is practically unchanged, deviations between the two cases grow for increasing incidence angles. This trend affects especially the branch of the propeller wake coming from the starboard/pressure side of the hydrofoil, developing on the side of negative $y$ coordinates. The spanwise elongation seen in Fig. 25 is partially replaced by the onset of an additional wake structure at the lower boundary of the wake, that is the tip vortex originating at the bottom end of the semi-infinite hydrofoil. However, the differences between the wake development downstream of the two hydrofoil geometries become much more obvious when the second-order statistics are considered.

Contours of the mean squares of the fluctuations in time of streamwise velocity are shown in Figs. 27 and 28. It should be noted that the latter are more noisy, due to the smaller size of the statistical sample, because of limitations of computational resources. It is worth recalling that the statistics from the present computations on the semi-infinite hydrofoil were computed across 10 revolutions, while those from our earlier simulations on the infinite hydrofoil were averaged across 40 revolutions. Nonetheless, they demonstrate negligible deviations between the two approximations of the rudder geometry at 0° incidence, corresponding to Fig. 27*a* and Fig. 28*a*. They become gradually more evident for increasing angles. In Fig. 27 the area of shear between the wake of the hydrofoil and that of the propeller is characterized by the highest levels of turbulent fluctuations, especially on the bottom side, were the most significant separation phenomena occurred upstream, resulting in a wider wake of the hydrofoil. The signature of the wake of the hydrofoil, ***HW***, is roughly aligned with its trailing edge, although it experiences a deflection, due to the azimuthal velocity within the wake of the propeller, directed towards the starboard side in the upper region and towards the port side in the lower region. The signature of the tip vortices from the propeller, ***PTV***, is located instead at the outer boundary of the propeller wake, that is on the port side in the upper region and the starboard side in the lower region. Although an additional vortex is shed from the bottom end of the semi-infinite hydrofoil, the velocity fluctuations are definitely lower in Fig. 28, due to the smaller size of the wake of the hydrofoil. This result is in line with the lower $SPLs$ from non-linear sources. As expected, no substantial deviations are visible on the side of positive $y$ coordinates between Figs. 27 and 28.

#### *4.3.3. Hydrophones at r/D=12 and z/D=1.0*

Moving away from the propeller–rudder system along the radial direction, the differences between cases of infinite and semi-infinite

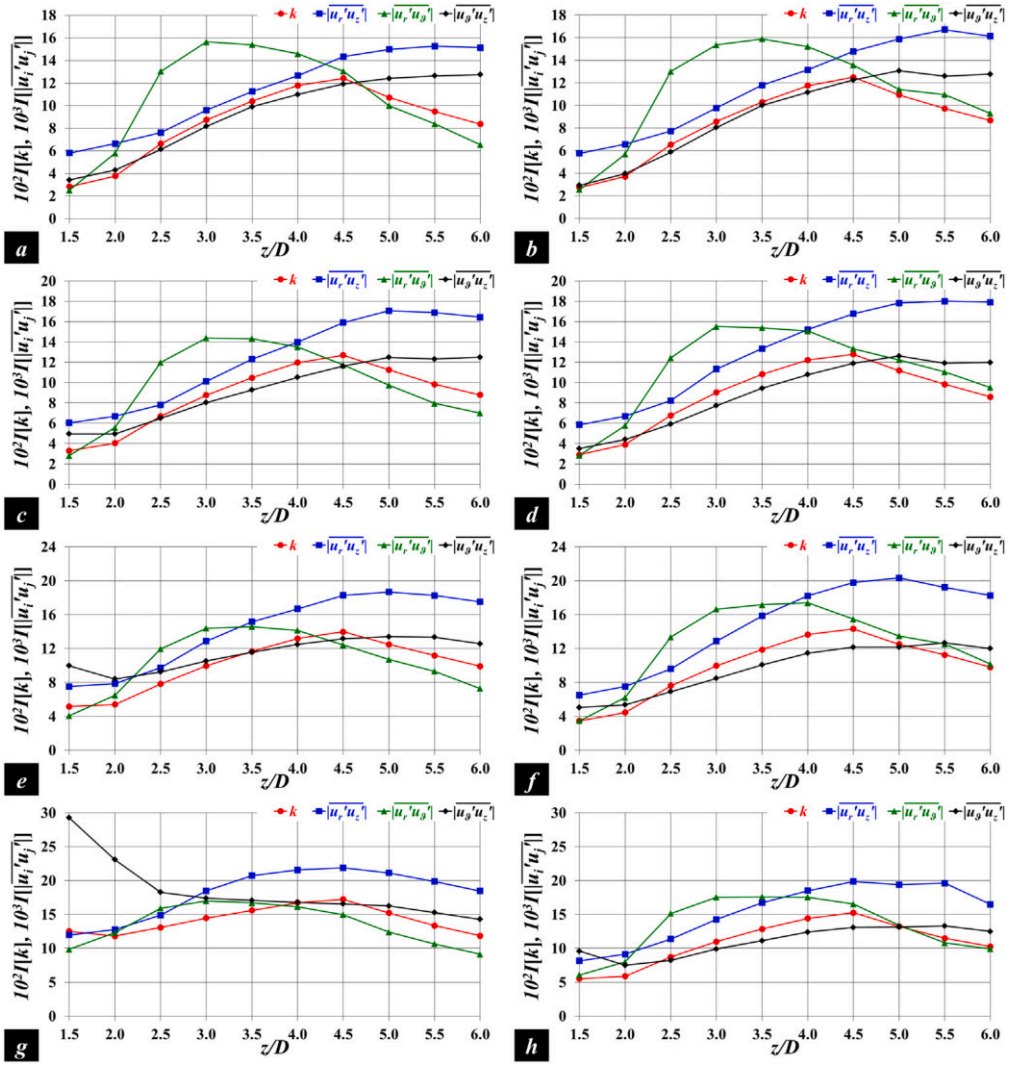


**Fig. 24.** Integrals of the turbulent stresses downstream of the (left panels) infinite and (right panels) semi-infinite hydrofoils in the configurations (*a*, *b*) ***I*00**, (*c*, *d*) ***I*05**, (*e*, *f*) ***I*10** and (*g*, *h*) ***I*15**. Values computed as in Eq. (14) and scaled by $U_\infty^2 \pi D^2/4$. Note the variation of the vertical scale from top to bottom.

hydrofoils become less obvious. Fig. 29 deals with the azimuthal averages across hydrophones of radial coordinate $r/D = 12$ and streamwise coordinate $z/D = 1.0$. Although deviations still exist between the two cases, they are a function of the particular frequency. Overall, in contrast with the results seen at smaller radial coordinates, the semi-infinite hydrofoil generates similar or even higher $SPLs$ than the infinite one. As discussed above, the latter is characterized by higher $SPLs$ coming from non-linear components. However, the quadrupole sound decays more quickly along the radial direction, making the linear sources the leading ones in defining the acoustic signature of the system, as shown in Fig. 30. While the non-linear component of sound, which is the leading one at small radial coordinates, is consistently higher from the infinite hydrofoil, this is not the case for the linear component.

The analysis reported in Section 4.3.1 revealed a significant growth of the thickness of the boundary layer on the suction side of the hydrofoil for large incidence angles, leading eventually to separation, affecting especially the side of negative $y$ coordinates of the infinite hydrofoil. These phenomena begin at outer spanwise coordinates, propagating towards the inner ones. In our earlier work (Posa et al., 2022d) on the infinite hydrofoil, we already found that the onset of separation actually results in lower levels of acoustic pressure, producing a decrease of the $SPLs$ from $\alpha = 10°$ to $\alpha = 15°$. This could be the result of the shift of the linear component of the acoustic signature towards higher frequencies, due to turbulence produced in the vicinity of the surface of the hydrofoil. The flow physics over the semi-infinite hydrofoil at large angles of incidence is much different: on the bottom side no separation occurs, even at the largest simulated angle. In addition, the momentum shifting from the pressure side towards the suction side through the tip of the hydrofoil is able to energize the suction side. These differences between the flow conditions on the suction side of the two hydrofoils are reinforced for increasing incidence angles, in agreement with the comparisons of their $SPLs$ in Fig. 31, where the polar plots deal with the $SPLs$ at the blade frequency at the hydrophones of radial and streamwise coordinates $r/D = 12$ and $z/D = 1.0$, respectively. A roughly dipolar distribution is generated,

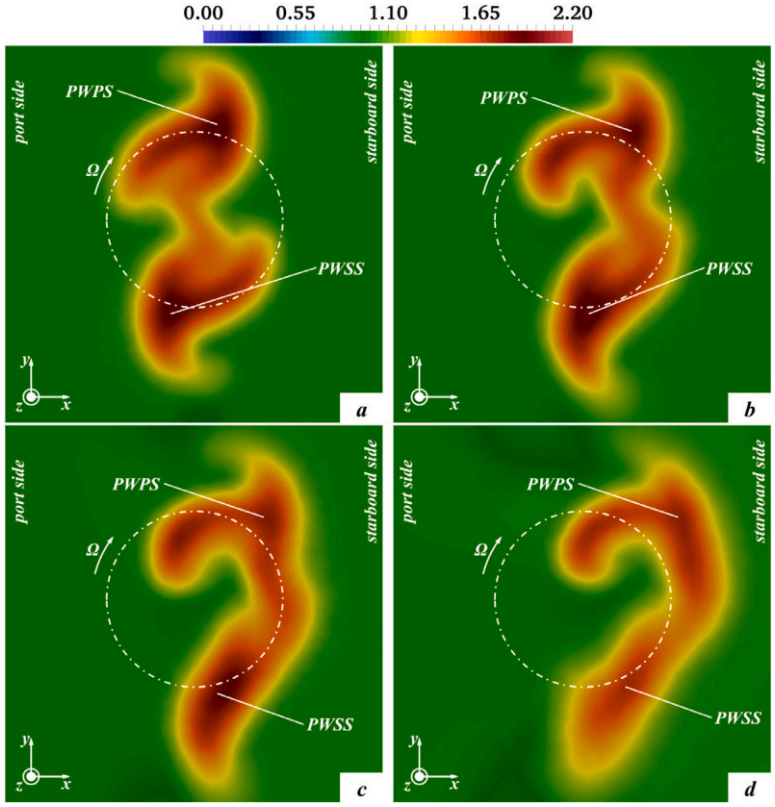


**Fig. 25.** Contours of time-averaged streamwise velocity, scaled by $U_\infty$, at $z/D = 4.0$, downstream of the infinite hydrofoil. Cases (*a*) ***I*00**, (*b*) ***I*05**, (*c*) ***I*10** and (*d*) ***I*15**. ***PWPS***: propeller wake from the port side of the hydrofoil. ***PWSS***: propeller wake from the starboard side of the hydrofoil. Dot-dashed line encompassing the projection of the area swept by the propeller blades.

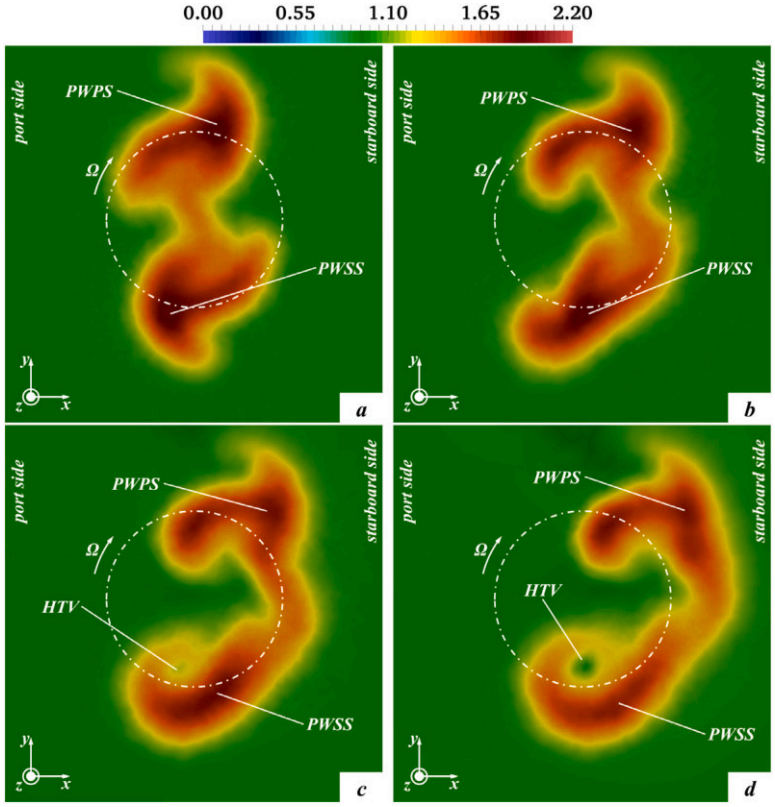


**Fig. 26.** Contours of time-averaged streamwise velocity, scaled by $U_\infty$, at $z/D = 4.0$, downstream of the semi-infinite hydrofoil. Cases (*a*) ***I*00**, (*b*) ***I*05**, (*c*) ***I*10** and (*d*) ***I*15**. ***PWPS***: propeller wake from the port side of the hydrofoil. ***PWSS***: propeller wake from the starboard side of the hydrofoil. ***HTV***: tip vortex from the hydrofoil. Dot-dashed line encompassing the projection of the area swept by the propeller blades.

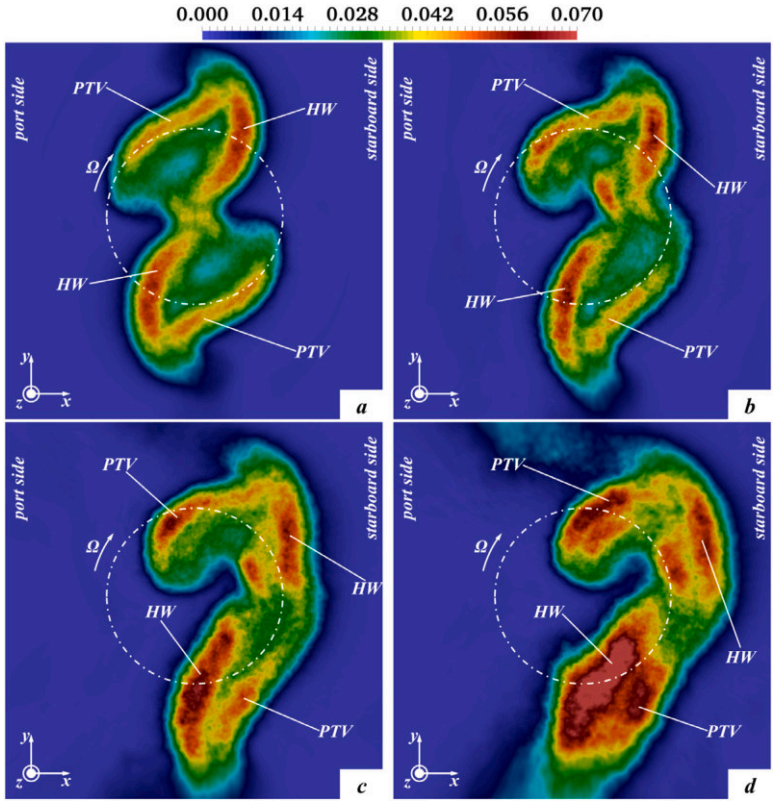


**Fig. 27.** Contours of the mean squares of the time-fluctuations of streamwise velocity, $\overline{u_z' u_z'}$, scaled by $U_\infty^2$, at $z/D = 4.0$, downstream of the infinite hydrofoil. Cases (*a*) ***I*00**, (*b*) ***I*05**, (*c*) ***I*10** and (*d*) ***I*15**. ***PTV***: tip vortices from the propeller. ***HW***: wake shed by the hydrofoil. Dot-dashed line encompassing the projection of the area swept by the propeller blades.

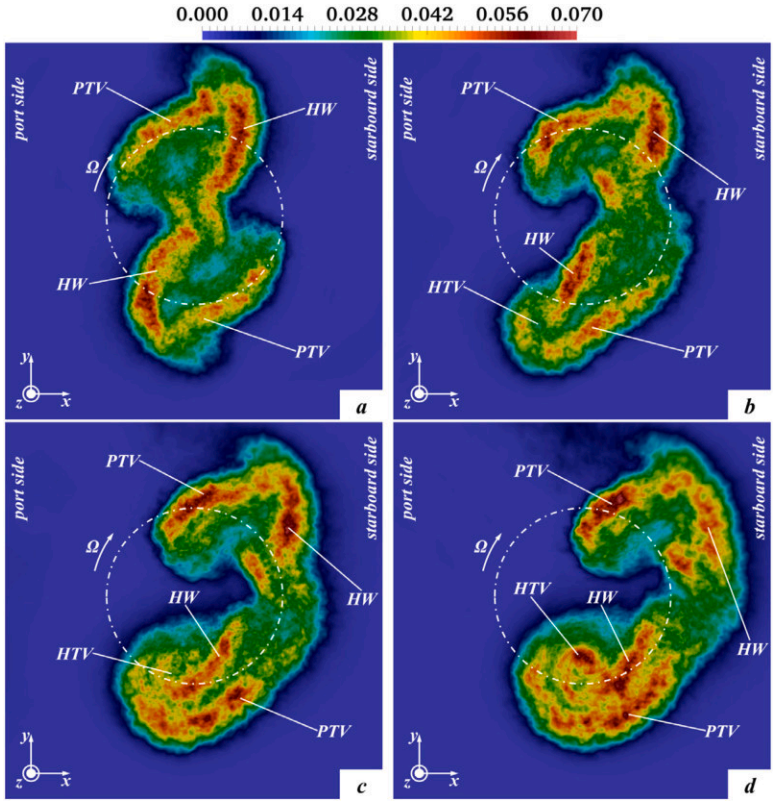


**Fig. 28.** Contours of the mean squares of the time-fluctuations of streamwise velocity, $\overline{u_z' u_z'}$, scaled by $U_\infty^2$, at $z/D = 4.0$, downstream of the semi-infinite hydrofoil. Cases (*a*) ***I*00**, (*b*) ***I*05**, (*c*) ***I*10** and (*d*) ***I*15**. ***PTV***: tip vortices from the propeller. ***HW***: wake shed by the hydrofoil. ***HTV***: tip vortex from the hydrofoil. Dot-dashed line encompassing the projection of the area swept by the propeller blades.

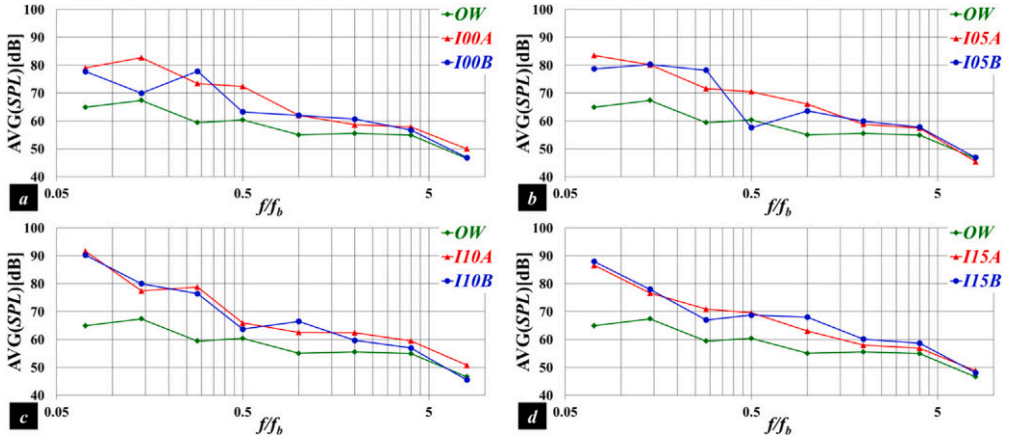


**Fig. 29.** Azimuthal averages of the $SPLs$ in third-octave bands at hydrophones of radial and axial coordinates $r/D = 12$ and $z/D = 1.0$, respectively: comparison between the simulations on the $(A)$ infinite and $(B)$ semi-infinite hydrofoils, including values in $(OW)$ open-water conditions. Cases $(a)$ ***I*00**, $(b)$ ***I*05**, $(c)$ ***I*10** and $(d)$ ***I*15**.

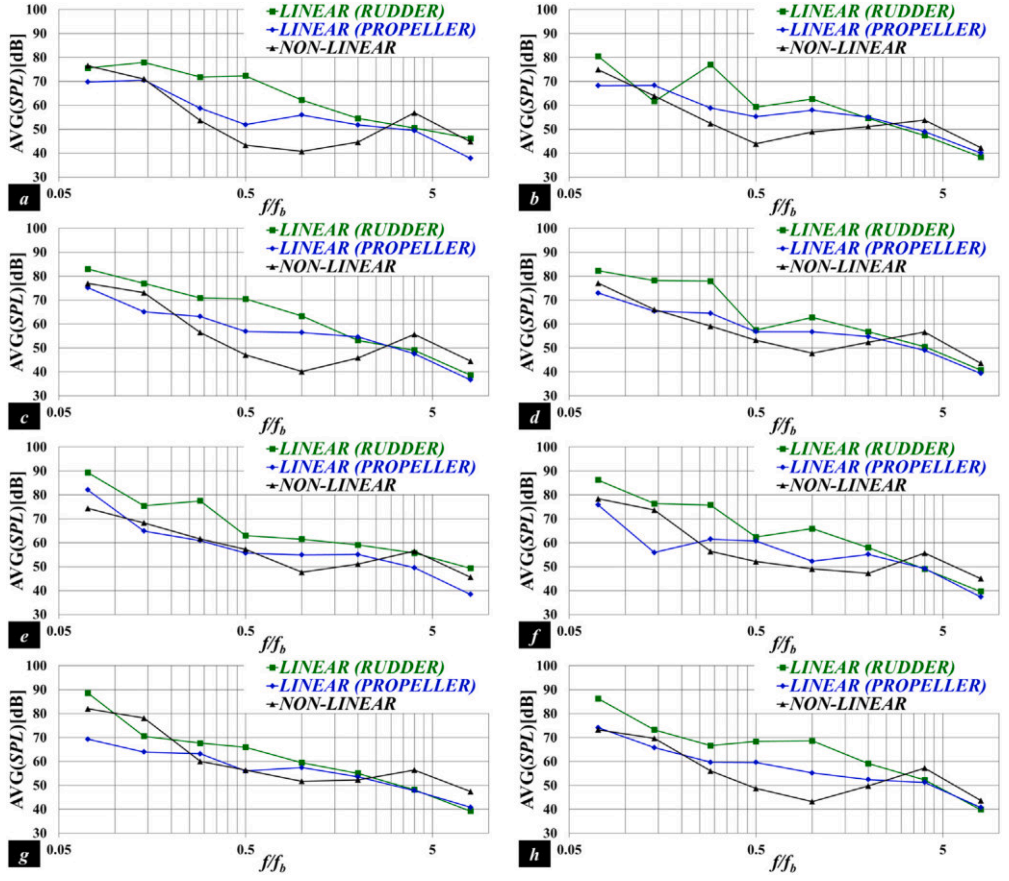


**Fig. 30.** Azimuthal averages of the $SPLs$ in third-octave bands at hydrophones of radial and axial coordinates $r/D = 12$ and $z/D = 1.0$, respectively: comparison across components of $SPLs$ between the simulations on the (left panels) infinite and (right panels) semi-infinite hydrofoils. Cases $(a, b)$ ***I*00**, $(c, d)$ ***I*05**, $(e, f)$ ***I*10** and $(g, h)$ ***I*15**.

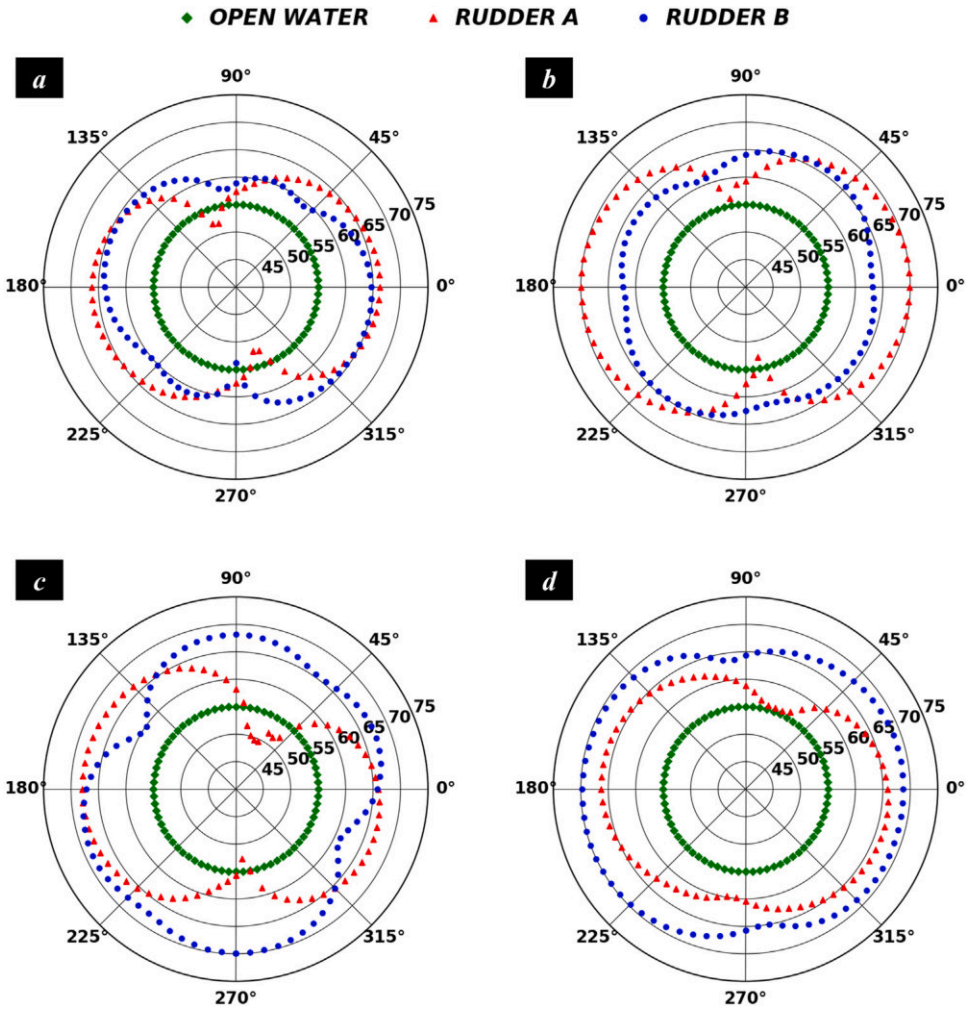


**Fig. 31.** Azimuthal distribution of the $SPLs$ in the third-octave band centered at the blade frequency at hydrophones of radial and axial coordinates $r/D = 12$ and $z/D = 1.0$, respectively: comparison between the simulations on the ($A$) infinite and ($B$) semi-infinite hydrofoils, including values in ($OW$) open-water conditions. Cases ($a$) ***I*00**, ($b$) ***I*05**, ($c$) ***I*10** and ($d$) ***I*15**.

which is due to the sound coming from the surface of the hydrofoil, the leading one. In agreement with the results at inner radii, while at the condition of no incidence, considered in Fig. 31$a$, the overall levels of acoustic pressure are similar between infinite and semi-infinite hydrofoils, this is increasingly not the case as the incidence angle grows. However, in this case this behavior is attributable to the linear component of sound, rather than to the non-linear one, as demonstrated above by means of Fig. 30. An additional, important difference, in comparison with the results seen at inner radial coordinates, is that larger incidence angles mainly result in higher $SPLs$ from the semi-infinite hydrofoil than from the infinite one. This is especially evident in Fig. 31$d$, referring to the case ***I*15**. Fig. 32, dealing with the $SPLs$ for ***I*15** across additional frequencies, confirms that higher levels of acoustic pressure come from the surface of the semi-infinite hydrofoil, in comparison with the infinite one. However, it is once again useful to remember that the limitations of the available database allowed us to explore only a range of rather low frequencies. Separation phenomena are instead expected to affect more the highest frequencies of the sound coming from the suction side of the hydrofoil, when separation occurs.

As discussed above, for increasing incidence angles a significant rise of the turbulent fluctuations in the vicinity of the surface of the hydrofoil occurs, affecting its port/suction side. This is demonstrated by the contours of the root mean squares of the fluctuations in time of the pressure coefficient, which affect the linear, loading component of the sound coming from the surface of the hydrofoil. They are shown at a distance from the port/suction side equal to 1%$c$ in Fig. 33, including isolines of $\overline{u}_z = 0$ on the surface of the hydrofoil, to indicate the position of boundary layer separation. From left to right in Fig. 33 the increase of the adverse streamwise pressure gradient promotes instability, leading to higher turbulent fluctuations and eventually to separation. This is especially the case of the top panels, dealing with the infinite hydrofoil: separation occurs more quickly on its bottom side, due to the upward shift of the propeller wake, which has the beneficial effect of stabilizing the boundary layer. As the propeller wake moves upwards, this beneficial effect is lost on the bottom side of the hydrofoil.

For the sake of completeness, similar contours are reported on the starboard/pressure side of the hydrofoils in Fig. 34. No isolines are

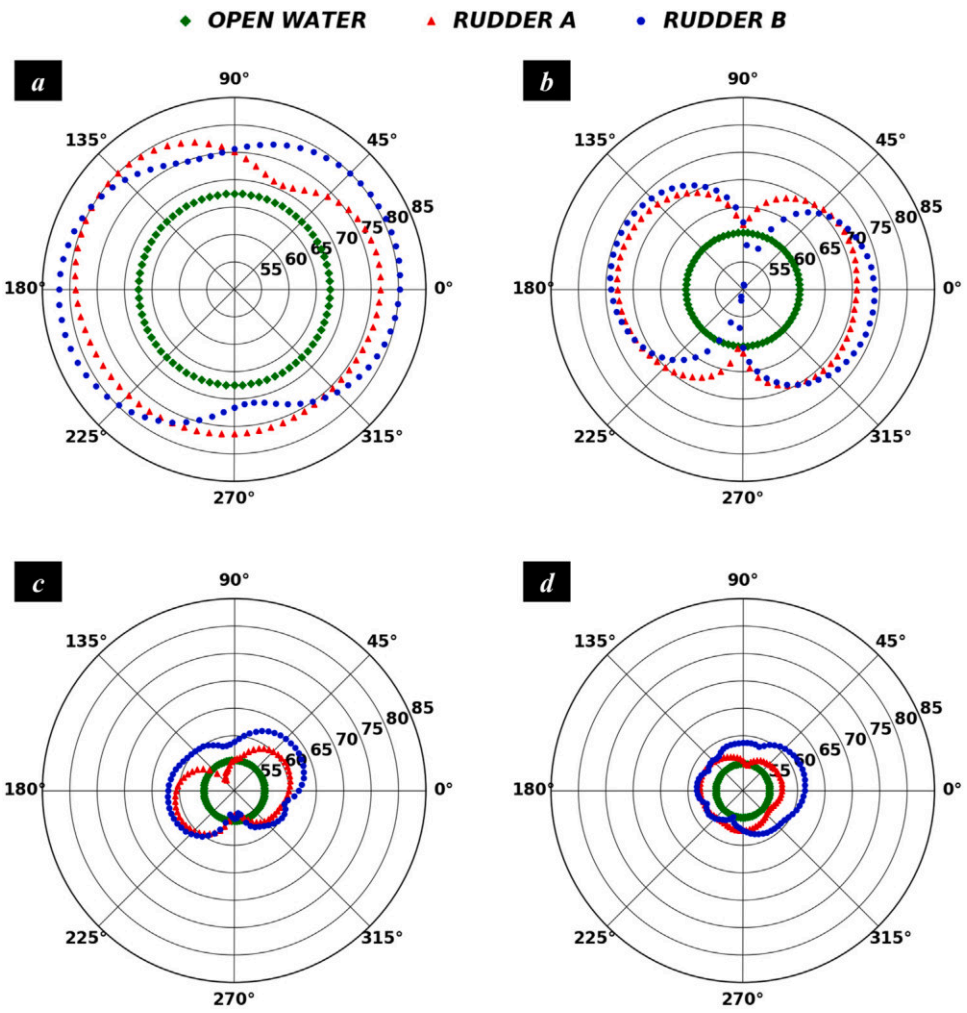


**Fig. 32.** Azimuthal distribution of the $SPLs$ in third-octave bands at hydrophones of radial and axial coordinates $r/D = 12$ and $z/D = 1.0$, respectively: comparison between the simulations on the $(A)$ infinite and $(B)$ semi-infinite hydrofoils, including values in $(OW)$ open-water conditions. Case ***I15***. Frequencies: $(a)$ $1.0f_s$, $(b)$ $0.5f_b$, $(c)$ $2.0f_b$, $(d)$ $4.0f_b$.

shown, since no separation phenomena occur, thanks to the favorable streamwise pressure gradient, which results in lower levels of pressure fluctuations than on the port side. In Fig. 34, the dependence of the contours on the incidence angle is much less obvious than in Fig. 33. Actually, the stabilizing pressure gradient has the effect of reducing the turbulent fluctuations. Meanwhile, as the incidence angle grows, the branch of the hub vortex from the propeller, impinging on the starboard side of the hydrofoil, becomes larger. In addition, the angle between the surface of the hydrofoil and the tip vortices from the propeller becomes smaller, increasing their shear. Both phenomena, which promote higher turbulence, roughly balance the stabilizing effect of the favorable pressure gradient, resulting in an overall weak dependence of the fluctuations of hydrodynamic pressure on the incidence angle.

## 5. Conclusions

Data from Large-Eddy Simulations, conducted on a cylindrical grid consisting of 3.8 billion points, were utilized to compare the acoustic signatures of two hydrofoils, mimicking simplified rudders working in the wake of a marine propeller. The results of the acoustic analysis from recent computations (Posa, 2022, 2023), dealing with a semi-infinite hydrofoil, were compared against those of our earlier studies on a hydrofoil of infinite spanwise extent (Posa et al., 2022b,d). Simplified rudders are often adopted in both experimental and numerical studies (Li 1996, Felli et al. 2009, 2011, 2013, 2014a,b, Felli and Falchi 2011, Felli 2020, Hu et al. 2019, 2021b, Wang et al. 2019) and the purpose of this work was to assess the influence of the two different approximations of the rudder geometry on the sound pressure levels. They were computed in post-processing, exploiting the Ffowcs-Williams & Hawkings acoustic analogy (Ffowcs-Williams and Hawkings, 1969). The overall approach was validated in our recent work (Posa et al., 2022c) against hydroacoustic measurements dealing with the same propeller in open-water conditions. For both hydrofoils four incidence angles were simulated, equivalent to 0°, 5°, 10° and 15°.

The major conclusions of the present study can be summarized as follows:

- ✓ Deviations between the two approximations of the rudder geometry were almost negligible at no incidence, becoming more significant at large incidence angles. Meanwhile, the increase of the sound pressure levels from the case of the isolated propeller was always substantial, as shown in Figs. 15, 16, 22 and 29, due to both the linear sources from the hydrofoil and the non-linear sources from the wake.
- ✓ As shown in Fig. 23, at small radii, in the vicinity of the propeller wake, the differences affecting the sound pressure levels at large angles were attributable especially to the non-linear sources, associated with a faster growth and eventual separation of the boundary layer on the suction side of the infinite hydrofoil.

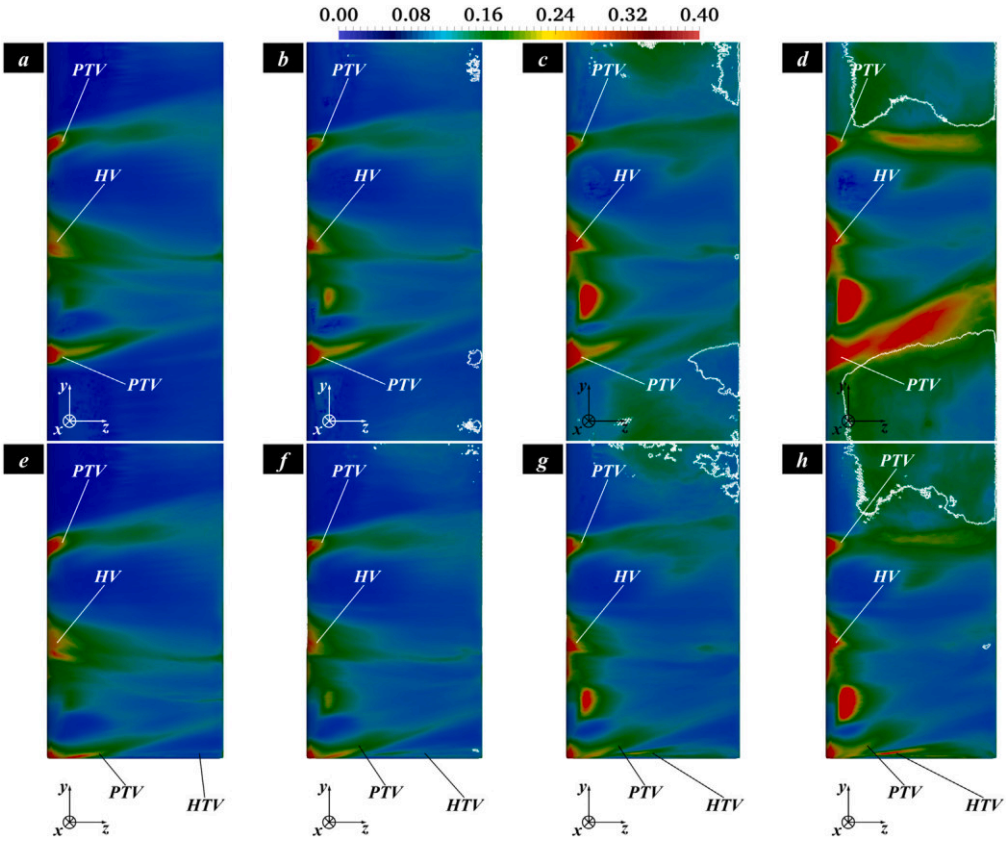


**Fig. 33.** Contours of the root mean squares of the time-fluctuations of pressure coefficient at a distance of $1\%c$ from the port side of the hydrofoil. Isolines for $\overline{u}_z = 0$ on the surface of the hydrofoil. Comparison between the simulations on the (top panels) infinite and (bottom panels) semi-infinite hydrofoils. Cases (*a*, *e*) ***I*00**, (*b*, *f*) ***I*05**, (*c*, *g*) ***I*10** and (*d*, *h*) ***I*15**. ***HV***: hub vortex from the propeller. ***PTV***: tip vortices from the propeller. ***HTV***: tip vortex from the hydrofoil.

- ✓ Moving downstream, the differences between the two acoustic signatures were reinforced, due to the growing importance of the non-linear sources of sound, because of wake instabilities and increasing turbulent stresses. This downstream growth of turbulence levels is thoroughly discussed in a number of earlier works on both the infinite (Posa et al. 2021, Posa and Broglia 2022a) and semi-infinite (Posa, 2023) approximations of the hydrofoil, as well as in Fig. 24.
- ✓ At outer radii the sound pressure levels from the semi-infinite hydrofoil became higher than those from the infinite one, especially for increasing incidence angles and large frequencies, due to the linear component of sound coming from the surface of the hydrofoil.
- ✓ Surprisingly, the substantial modification of the flow physics associated with separation phenomena, although producing higher fluctuations of hydrodynamic pressure on the suction side of the hydrofoil, resulted in lower overall sound pressure levels: this result was verified by both comparisons across incidence angles for the infinite hydrofoil and comparisons between hydrofoil geometries at the largest, simulated angle. Considering the available database, this result may be attributed to the focus of the present study towards low frequencies, associated with the periodic impingement of the propeller wake on the surface of the hydrofoil, while separation is likely to affect more higher frequencies.

To summarize, this study pointed out that the influence of different approximations of the spanwise extent of the rudder on its acoustic signature, negligible at 0° incidence, becomes significant at large angles. This conclusion suggests that simplified, infinite approximations of the geometry of actual rudders, often utilized in the literature on propeller–rudder interaction, are accurate enough at working conditions close to design. In contrast, they are expected to affect substantially the relevant acoustic phenomena if the analysis is oriented towards more challenging working conditions, as in this case, where the orientation of the hydrofoil at large angles of incidence gives rise to significant pressure gradients across the streamwise direction and between port and starboard sides, able to trigger phenomena of boundary layer separation and large tip vortices from the ends of rudders.

## CRediT authorship contribution statement

**Antonio Posa:** Conceptualization, Methodology, Software, Validation, Formal analysis, Investigation, Resources, Data curation, Writing – original draft, Writing – review & editing, Visualization, Supervision. **Riccardo Broglia:** Conceptualization, Resources, Writing – review & editing. **Elias Balaras:** Methodology, Software, Writing – review & editing. **Mario Felli:** Conceptualization, Validation, Writing – review & editing, Project administration, Funding acquisition.

## Declaration of competing interest

The authors declare that they have no known competing financial interests or personal relationships that could have appeared to influence the work reported in this paper.

## Data availability

Data will be made available on request.

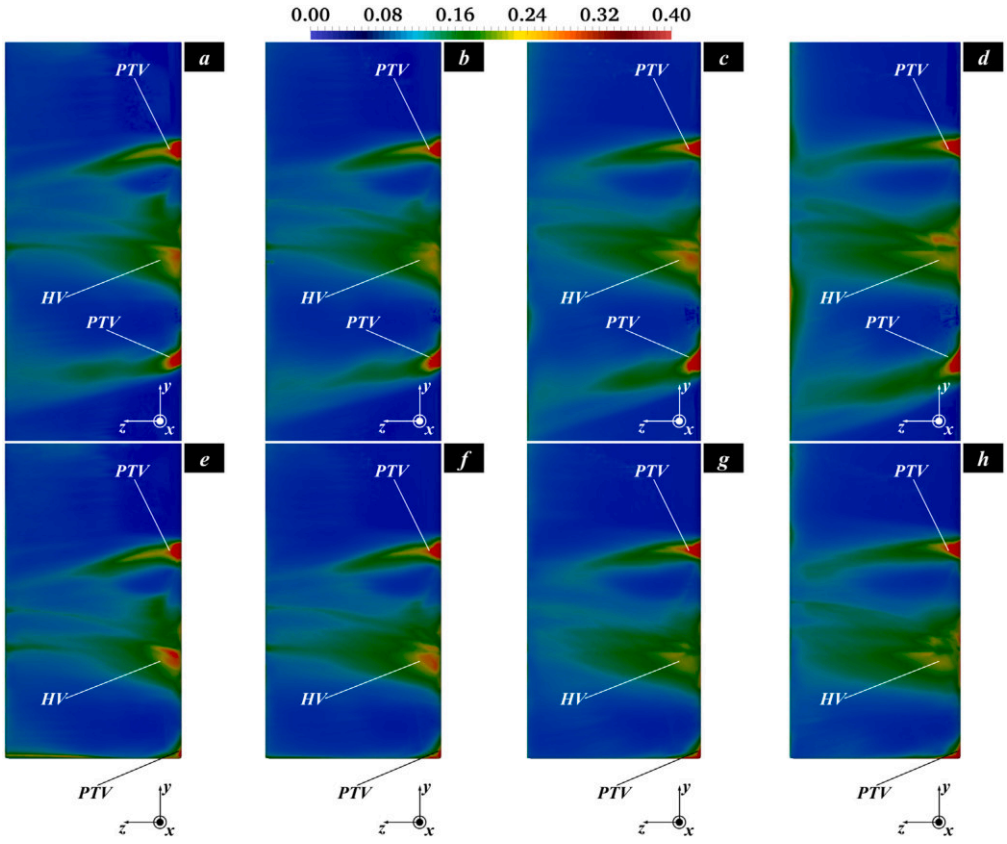


**Fig. 34.** Contours of the root mean squares of the time-fluctuations of pressure coefficient at a distance of $1\%c$ from the starboard side of the hydrofoil. Comparison between the simulations on the (top panels) infinite and (bottom panels) semi-infinite hydrofoils. Cases (*a*, *e*) ***I*00**, (*b*, *f*) ***I*05**, (*c*, *g*) ***I*10** and (*d*, *h*) ***I*15**. ***HV***: hub vortex from the propeller. ***PTV***: tip vortices from the propeller.

## Acknowledgments

This study was funded by the European Union's Horizon 2020 research and innovation programme under grant agreement N. 10100 6443 (SATURN, Developing solutions to underwater radiated noise).

We are grateful to Michael Brown (Naval Surface Warfare Center, Carderock Division, Maryland) for generating the Lagrangian grid of the INSEAN E1658 propeller and to Massimiliano Guarrasi and Debora Testi (CINECA) for their support for access to HPC resources and data storage. We acknowledge PRACE for awarding us access to Marconi KNL at CINECA (Italy) and Joliot-Curie Rome at GENCI/CEA (France), with allocations granted to the projects "LES of the Interaction Between a Rudder and the Wake of a Propeller" (proposal n. 2018184409) and "Characterization of the wake of a propeller–rudder system" (proposal n. 2020225357) in the framework of the 17th and 21st PRACE Calls for Proposals for Project Access.

## References

Bensow, R., Liefvendahl, M., 2016. An acoustic analogy and scale-resolving flow simulation methodology for the prediction of propeller radiated noise. In: Proceedings of the 31st Symposium on Naval Hydrodynamics. 11-16 September 2016, Monterey, CA, USA.

Chen, M., Liu, J., Si, Q., Liang, Y., Jin, Z., Yuan, J., 2022. Investigation into the hydrodynamic noise characteristics of electric ducted propeller. J. Mar. Sci. Eng. 10 (3), 378.

Chou, E., Southall, B., Robards, M., Rosenbaum, H., 2021. International policy, recommendations, actions and mitigation efforts of anthropogenic underwater noise. Ocean Coast. Manag. 202, 105427.

Cianferra, M., Armenio, V., 2021. Scaling properties of the Ffowcs-Williams and Hawkings equation for complex acoustic source close to a free surface. J. Fluid Mech. 927, A2.

Cianferra, M., Petronio, A., Armenio, V., 2018. Hydrodynamic noise from a propeller in open sea condition. In: Technology and Science for the Ships of the Future - Proceedings of NAV 2018: 19th International Conference on Ship and Maritime Research. pp. 149–156.

Cianferra, M., Petronio, A., Armenio, V., 2019a. Non-linear noise from a ship propeller in open sea condition. Ocean Eng. 191, 106474.

Cianferra, M., Petronio, A., Armenio, V., 2019b. Numerical prediction of ship propeller noise through acoustic analogy. In: Sixth International Symposium on Marine Propulsors. SMP19, Rome, Italy, May 2019.

Di Francescantonio, P., 1997. A new boundary integral formulation for the prediction of sound radiation. J. Sound Vib. 202 (4), 491–509.

Di Franco, E., Pierson, P., Di Iorio, L., Calò, A., Cottalorda, J., Derijard, B., Di Franco, A., Galvé, A., Guibbolini, M., Lebrun, J., Micheli, F., Priouzeau, F., Risso-de Faverney, C., Rossi, F., Sabourault, C., Spennato, G., Verrando, P., Guidetti, P., 2020. Effects of marine noise pollution on Mediterranean fishes and invertebrates: A review. Mar. Pollut. Bull. 159, 111450.

Felli, M., 2020. Underlying mechanisms of propeller wake interaction with a wing. J. Fluid Mech. 908, A10.

Felli, M., Camussi, R., Guj, G., 2009. Experimental analysis of the flow field around a propeller-rudder configuration. Exp. Fluids 46 (1), 147–164.

Felli, M., Falchi, M., 2011. Propeller tip and hub vortex dynamics in the interaction with a rudder. Exp. Fluids 51 (5), 1385.

Felli, M., Falchi, M., 2018. A parametric survey of propeller wake instability mechanisms by detailed flow measurement and time resolved visualizations. In: 32nd Symposium on Naval Hydrodynamics. 5-10 August 2018, Hamburg, Germany.

Felli, M., Falchi, M., Dubbioso, G., 2015. Experimental approaches for the diagnostics of hydroacoustic problems in naval propulsion. Ocean Eng. 106, 1–19.

Felli, M., Falchi, M., Pereira, F., 2011. Investigation of the Flow Field around a Propeller-Rudder Configuration: On-Surface Pressure Measurements and Velocity-Pressure-Phase-Locked Correlations. In: Second International Symposium on Marine Propulsors. SMP11, Hamburg, Germany, June 2011.

Felli, M., Grizzi, S., Falchi, M., 2013. Hydroacoustic and hydrodynamic analysis of a propeller-rudder configuration by pressure signal wavelet decomposition and optical techniques. In: Third International Symposium on Marine Propulsors. Launceston, Australia, May 2013.

Felli, M., Grizzi, S., Falchi, M., 2014a. A novel approach for the isolation of the sound and pseudo-sound contributions from near-field pressure fluctuation measurements:

Analysis of the hydroacoustic and hydrodynamic perturbation in a propeller-rudder system. Exp. Fluids 55 (1), 1651.
Felli, M., Grizzi, S., Falchi, M., 2014b. Hydrodynamic and Hydroacoustic Phenomena in the Propeller Wake-Rudder Interaction. In: Thirty-Third International Conference on Offshore Mechanics and Arctic Engineering. OMAE 2014, San Francisco, California, USA, June 2014.
Ffowcs-Williams, J.E., Hawkings, D.L., 1969. Sound generation by turbulence and surfaces in arbitrary motion. Philos. Trans. R. Soc. London. Ser. A, Math. Phys. Sci. 264 (1151), 321–342.
Ge, M., Svennberg, U., Bensow, R., 2022. Investigations on prediction of ship noise using the FWH acoustic analogy with incompressible flow input. Ocean Eng. 257, 111531.
Guo, H., Guo, C., Hu, J., Lin, J., Zhong, X., 2021. Influence of jet flow on the hydrodynamic and noise performance of propeller. Phys. Fluids 33 (6), 065123.
Hu, J., Ning, X., Zhao, W., Li, F., Ma, J., Zhang, W., Sun, S., Zou, M., Lin, C., 2021a. Numerical simulation of the cavitating noise of contra-rotating propellers based on detached eddy simulation and the Ffowcs Williams-Hawkings acoustics equation. Phys. Fluids 33 (11), 115117.
Hu, J., Zhang, W., Guo, H., Sun, S., Chen, F., Guo, C., 2021b. Numerical simulation of propeller wake vortex-rudder interaction in oblique flows. Ships Offshore Struct. 16 (2), 144–155.
Hu, J., Zhang, W., Sun, S., Guo, C., 2019. Numerical simulation of Vortex-Rudder interactions behind the propeller. Ocean Eng. 190, 106446.
Ianniello, S., 2016. The Ffowcs Williams-Hawkings equation for hydroacoustic analysis of rotating blades. Part 1. The rotpole. J. Fluid Mech. 797, 345–388.
Ianniello, S., Muscari, R., Di Mascio, A., 2013. Ship underwater noise assessment by the acoustic analogy. Part I: Nonlinear analysis of a marine propeller in a uniform flow. J. Mar. Sci. Technol. (Japan) 18 (4), 547–570.
Ianniello, S., Muscari, R., Di Mascio, A., 2014. Ship underwater noise assessment by the acoustic analogy, part III: Measurements versus numerical predictions on a full-scale ship. J. Mar. Sci. Technol. (Japan) 19 (2), 125–142.
Ianniello, S., Testa, C., 2019. An overview on the use of the Ffowcs Williams-Hawkings equation for the hydroacoustic analysis of marine propellers. In: VIII International Conference on Computational Methods in Marine Engineering. MARINE 2019, GÖTeborg, Sweden, 13-15 May 2019.
Jeong, J., Hussain, F., 1995. On the identification of a vortex. J. Fluid Mech. 285, 69–94.
Keller, J., Kumar, P., Mahesh, K., 2018. Examination of propeller sound production using large eddy simulation. Phys. Rev. Fluids 3 (6), 064601.
Kim, S., Kinnas, S., 2022. Numerical prediction of propeller-induced noise in open water and ship behind conditions. Ocean Eng. 261, 112122.
Kim, I., Yoon, D., Jeong, J., Kim, S., You, D., 2023. Domain reduction strategy for large-eddy simulation to predict underwater radiated noise from a marine propeller. Ocean Eng. 279, 114538.
Kimmerl, J., Abdel-Maksoud, M., 2023. Visualization of Underwater Radiated Noise in the Near-and Far-Field of a Propeller-Hull Configuration Using CFD Simulation Results. J. Mar. Sci. Eng. 11 (4), 834.
Kimmerl, J., Mertes, P., Abdel-Maksoud, M., 2021. Application of large eddy simulation to predict underwater noise of marine propulsors. Part 2: Noise generation. J. Mar. Sci. Eng. 9 (7), 778.
Ku, G., Cho, J., Cheong, C., Seol, H., 2021. Numerical investigation of tip-vortex cavitation noise of submarine propellers using hybrid computational hydro-acoustic approach. Ocean Eng. 238, 109693.
Li, D.-Q., 1996. A non-linear method for the propeller-rudder interaction with the slipstream deformation taken into account. Comput. Methods Appl. Mech. Engrg. 130 (1–2), 115–132.
Lidtke, A., Humphrey, V., Turnock, S., 2016. Feasibility study into a computational approach for marine propeller noise and cavitation modelling. Ocean Eng. 120, 152–159.
Lidtke, A., Lloyd, T., Lafeber, F., Bosschers, J., 2022. Predicting cavitating propeller noise in off-design conditions using scale-resolving CFD simulations. Ocean Eng. 254, 111176.
Lidtke, A., Lloyd, T., Vaz, G., 2019. Acoustic modelling of a propeller subject to non-uniform inflow. In: Proceedings of the Sixth International Symposium on Marine Propulsors. SMP19, Rome, Italy, May 2019.
Lidtke, A., Turnock, S., Humphrey, V., 2015. Use of acoustic analogy for marine propeller noise characterisation. In: Proceedings of the Fourth International Symposium on Marine Propulsors. SMP15, Austin, Texas, June 2015.
Liefvendahl, M., Lane, G., Winroth, M., Croaker, P., 2022. Wall-pressure fluctuations from wall-modelled large-eddy simulations. In: Proceedings of the 34th Symposium on Naval Hydrodynamics. 26 June - 1 July 2022, Washington, DC, USA.
Lighthill, M., 1952. On sound generated aerodynamically I. General theory. Proc. R. Soc. London. Ser. A. Math. Phys. Sci. 211 (1107), 564–587.
Masud, N., Hayes, L., Crivelli, D., Grigg, S., Cable, J., 2020. Noise pollution: Acute noise exposure increases susceptibility to disease and chronic exposure reduces host survival: Noise pollution and disease resistance. R. Soc. Open Sci. 7 (9), 200172.
McIntyre, D., Rahimpour, M., Dong, Z., Tani, G., Miglianti, F., Viviani, M., Oshkai, P., 2022. Experimental measurements and numerical simulations of underwater radiated noise from a model-scale propeller in uniform inflow. Ocean Eng. 255, 111409.
Merchant, N., 2019. Underwater noise abatement: Economic factors and policy options. Environ. Sci. Policy 92, 116–123.
Nicoud, F., Ducros, F., 1999. Subgrid-scale stress modelling based on the square of the velocity gradient tensor. Flow Turbul. Combust. 62 (3), 183–200.
Petris, G., Cianferra, M., Armenio, V., 2022. Marine propeller noise propagation within bounded domains. Ocean Eng. 265, 112618.
Posa, A., 2022. Tip vortices shed by a hydrofoil in the wake of a marine propeller. Phys. Fluids 34 (12), 125134.
Posa, A., 2023. End effects in the wake of a hydrofoil working downstream of a propeller. Phys. Fluids 35 (4), 045122.
Posa, A., Balaras, E., 2016. A numerical investigation of the wake of an axisymmetric body with appendages. J. Fluid Mech. 792, 470–498.
Posa, A., Balaras, E., 2018. Large-Eddy Simulations of a notional submarine in towed and self-propelled configurations. Comput. & Fluids 165, 116–126.
Posa, A., Balaras, E., 2020. A numerical investigation about the effects of Reynolds number on the flow around an appended axisymmetric body of revolution. J. Fluid Mech. 884, A41.
Posa, A., Broglia, R., 2021. Flow over a hydrofoil at incidence immersed within the wake of a propeller. Phys. Fluids 33 (12), 125108.
Posa, A., Broglia, R., 2022a. Development of the wake shed by a system composed of a propeller and a rudder at incidence. Int. J. Heat Fluid Flow 94, 108919.
Posa, A., Broglia, R., 2022b. Near wake of a propeller across a hydrofoil at incidence. Phys. Fluids 34 (6), 065141.
Posa, A., Broglia, R., 2022c. Spanwise distribution of the loads on a hydrofoil working in the wake of an upstream propeller. Ocean Eng. 264, 112542.
Posa, A., Broglia, R., Balaras, E., 2019a. LES study of the wake features of a propeller in presence of an upstream rudder. Comput. & Fluids 192, 104247.
Posa, A., Broglia, R., Balaras, E., 2020. The wake structure of a propeller operating upstream of a hydrofoil. J. Fluid Mech. 904, A12.
Posa, A., Broglia, R., Balaras, E., 2021. The wake flow downstream of a propeller-rudder system. Int. J. Heat Fluid Flow 87, 108765.
Posa, A., Broglia, R., Balaras, E., 2022a. The dynamics of the tip and hub vortices shed by a propeller: Eulerian and Lagrangian approaches. Comput. & Fluids 236, 105313.
Posa, A., Broglia, R., Balaras, E., Felli, M., 2023. The acoustic signature of a propeller-hydrofoil system in the far field. Phys. Fluids 35 (7), 075101.
Posa, A., Broglia, R., Felli, M., 2022b. Acoustic signature of a propeller operating upstream of a hydrofoil. Phys. Fluids 34 (6), 065132.
Posa, A., Broglia, R., Felli, M., Cianferra, M., Armenio, V., 2022c. Hydroacoustic analysis of a marine propeller using large-eddy simulation and acoustic analogy. J. Fluid Mech. 947, A46.
Posa, A., Broglia, R., Felli, M., Falchi, M., Balaras, E., 2019b. Characterization of the wake of a submarine propeller via Large-Eddy Simulation. Comput. & Fluids 184, 138–152.
Posa, A., Felli, M., Broglia, R., 2022d. The signature of a propeller-rudder system: Acoustic analogy based on LES data. Ocean Eng. 259, 112059.
Qin, D., Pan, G., Lee, S., Huang, Q., Shi, Y., 2019. Underwater radiated noise reduction technology using sawtooth duct for pumpjet propulsor. Ocean Eng. 188, 106228.
Rossi, T., Toivanen, J., 1999. A parallel fast direct solver for block tridiagonal systems with separable matrices of arbitrary dimension. SIAM J. Sci. Comput. 20 (5), 1778–1793.
Sakamoto, N., Kamiirisa, H., 2018. Prediction of near field propeller cavitation noise by viscous CFD with semi-empirical approach and its validation in model and full scale. Ocean Eng. 168, 41–59.
Sezen, S., Atlar, M., 2022a. Marine propeller underwater radiated noise prediction with the FWH acoustic analogy part 3: Assessment of full-scale propeller hydroacoustic performance versus sea trial data. Ocean Eng. 266, 112712.
Sezen, S., Atlar, M., 2022b. Numerical investigation into the effects of tip vortex cavitation on propeller underwater radiated noise (URN) using a hybrid CFD method. Ocean Eng. 112658.
Sezen, S., Atlar, M., 2023. Marine propeller underwater radiated noise prediction with the FWH acoustic analogy Part 2: Assessment of model scale propeller hydroacoustic performance under non-uniform flow conditions. Ocean Eng. 270.
Sezen, S., Atlar, M., Fitzsimmons, P., 2021a. Prediction of cavitating propeller underwater radiated noise using RANS & DES-based hybrid method. Ships Offshore Struct. 16 (S1), 93–105.
Sezen, S., Cosgun, T., Yurtseven, A., Atlar, M., 2021b. Numerical investigation of marine propeller Underwater Radiated Noise using acoustic analogy part 1: The influence of grid resolution. Ocean Eng. 220, 108448.
Sezen, S., Cosgun, T., Yurtseven, A., Atlar, M., 2021c. Numerical investigation of marine propeller underwater radiated noise using acoustic analogy Part 2: The influence of eddy viscosity turbulence models. Ocean Eng. 220, 108353.
Sezen, S., Kinaci, O., 2019. Incompressible flow assumption in hydroacoustic predictions of marine propellers. Ocean Eng. 186, 106138.
Sezen, S., Uzun, D., Ozyurt, R., Turan, O., Atlar, M., 2021d. Effect of biofouling roughness on a marine propeller's performance including cavitation and underwater radiated noise (URN). Appl. Ocean Res. 107, 102491.
Smith, T., Rigby, J., 2022. Underwater radiated noise from marine vessels: A review of noise reduction methods and technology. Ocean Eng. 266, 112863.

Tani, G., Viviani, M., Felli, M., Lafeber, F., Lloyd, T., Aktas, B., Atlar, M., Turkmen, S., Seol, H., Hallander, J., Sakamoto, N., 2020. Noise measurements of a cavitating propeller in different facilities: Results of the round Robin test programme. Ocean Eng. 213, 107599.

Testa, C., Porcacchia, F., Zaghi, S., Gennaretti, M., 2021. Study of a FWH-based permeable-surface formulation for propeller hydroacoustics. Ocean Eng. 240, 109828.

Vakili, S., Ölçer, A., Ballini, F., 2021. The development of a transdisciplinary policy framework for shipping companies to mitigate underwater noise pollution from commercial vessels. Mar. Pollut. Bull. 171, 112687.

Van Kan, J.J.I.M., 1986. A second-order accurate pressure-correction scheme for viscous incompressible flow. SIAM J. Sci. Stat. Comput. 7 (3), 870–891.

Viitanen, V., Hynninen, A., Sipilä, T., Siikonen, T., 2018. DDES of wetted and cavitating marine propeller for CHA underwater noise assessment. J. Mar. Sci. Eng. 6 (2), 56.

Wang, Z.-T., Duan, P.-X., Wang, K.-X., Wang, D., 2021. Noise pollution disrupts freshwater cetaceans. Science 374 (6573), 1332–1333.

Wang, L., Guo, C., Xu, P., Su, Y., 2019. Analysis of the wake dynamics of a propeller operating before a rudder. Ocean Eng. 188, 106250.

Yang, J., Balaras, E., 2006. An embedded-boundary formulation for large-eddy simulation of turbulent flows interacting with moving boundaries. J. Comput. Phys. 215 (1), 12–40.

Yu, K., Park, D., Choi, J., Seol, H., Park, I., Lee, S., 2023. Effect of skew on the tonal noise characteristics of a full-scale submarine propeller. Ocean Eng. 276, 114218.

Zhou, Z., Liu, Y., Wang, H., Wang, S., 2023. Mass-conserved solution to the Ffowcs-Williams and Hawkings equation for compact source regions. Aerospace 10 (2), 148.

Zhou, Z., Wang, H., Wang, S., 2021a. Simplified permeable surface correction for frequency-domain Ffowcs Williams and Hawkings integrals. Theor. Appl. Mech. Lett. 11 (4), 100259.

Zhou, Z., Wang, H., Wang, S., He, G., 2021b. Lighthill stress flux model for Ffowcs Williams-Hawkings integrals in frequency domain. AIAA J. 59 (11), 4809–4814.

Zhou, Z., Zang, Z., Wang, H., Wang, S., 2022. Far-field approximations to the derivatives of Green's function for the Ffowcs Williams and Hawkings equation. Adv. Aerodyn. 4 (1), 12.